MRI of the Lungs Using Hyperpolarized Noble Gases

Harald E. Möller,[1*] X. Josette Chen,[2] Brian Saam,[3] Klaus D. Hagspiel,[4] G. Allan Johnson,[5] Talissa A. Altes,[4] Eduard E. de Lange,[4] and Hans-Ulrich Kauczor[6]

The nuclear spin polarization of the noble gas isotopes ^{3}He and ^{129}Xe can be increased using optical pumping methods by four to five orders of magnitude. This extraordinary gain in polarization translates directly into a gain in signal strength for MRI. The new technology of hyperpolarized (HP) gas MRI holds enormous potential for enhancing sensitivity and contrast in pulmonary imaging. This review outlines the physics underlying the optical pumping process, imaging strategies coping with the nonequilibrium polarization, and effects of the alveolar microstructure on relaxation and diffusion of the noble gases. It presents recent progress in HP gas MRI and applications ranging from MR microscopy of airspaces to imaging pulmonary function in patients and suggests potential directions for future developments.   Magn Reson Med 47:1029–1051, 2002. © 2002 Wiley-Liss, Inc.

Key words: hyperpolarized ^{3}He; hyperpolarized ^{129}Xe; lung; perfusion; ventilation

MRI has been extremely successful at diagnosing soft tissue disease since its discovery in 1972 (1). However, MRI is not as sensitive in comparison with other biomedical imaging techniques, such as CT, positron-emission tomography, or single-photon emission computed tomography. This is a consequence of a very small signal from a small population difference between nuclear energy states. For a spin-1/2 system, the "nuclear spin polarization", P_N, is defined as:

$$P_N = \frac{|N_+ - N_-|}{N_+ + N_-} = \frac{|N_+ - N_-|}{N},$$ [1]

where N_+ and N_- denote populations with magnetic spin quantum numbers $+1/2$ and $-1/2$, respectively. Typically,

[1]Max-Planck-Institut für neuropsychologische Forschung, Leipzig, Germany.
[2]Sunnybrook & Women's College Health Sciences Centre, University of Toronto, Toronto, Ontario, Canada.
[3]Department of Physics, University of Utah, Salt Lake City, Utah.
[4]Department of Radiology, University of Virginia Health Sciences Center, Charlottesville, Virginia.
[5]Center for In Vivo Microscopy, Duke University Medical Center, Durham, North Carolina.
[6]Klinik für Radiologie, Johannes-Gutenberg-Universität Mainz, Mainz, Germany.

*Correspondence to: Harald E. Möller, Ph.D., Max Planck Institute of Cognitive Neuroscience, Stephanstraβe 1a, D-04103 Leipzig, Germany. E-mail: moeller@cns.mpg.de

the thermal energy of the sample at temperature T exceeds the energy difference between the nuclear spin states in a magnetic field B_0 by several orders of magnitude ("high-temperature approximation") and the equilibrium polarization can be written as:

$$P_{N,0} \approx \frac{|\gamma|\hbar B_0}{2k_B T},$$ [2]

where γ is the magnetogyric ratio, $\hbar$ is Planck's constant divided by 2π, and k_B is Boltzmann's constant. As an example, $P_{N,0} \approx 5$ ppm is predicted with Eq. [2] for protons (^{1}H) at body temperature ($T = 37°C$) and $B_0 = 1.5$T. In view of the inherent sensitivity problem, increasing the signal-to-noise ratio (SNR) has been a field of continuous research since the discovery of NMR.

Recently, the use of optically polarized noble gas isotopes ^{3}He and ^{129}Xe has attracted increasing interest for use in a variety of promising MR applications. These systems exhibit polarizations exceeding the thermal levels by several orders of magnitude. While the use of such "hyperpolarized" (HP) gases for MRI is a recent development, it is based on a solid foundation of work in atomic physics. The groundwork was laid by Kastler (2) more than 50 years ago by demonstrating transfer of angular momentum from circularly polarized light to the electron and nuclear spins of atoms, a process called "optical pumping" (OP). Since 1991, exploitation of OP as a means of enhancing signal initiated the development of a novel field in NMR (3,4). Research involving HP noble gases has been exceptionally fruitful in biomedical MRI as well as providing applications for investigation of materials (5–8).

In the context of proton MRI, the lung is a particularly challenging area to study (9). Even at end expiration, the overall density is only ~0.30 g/cm³; hence, the water content is low. Regarding this obstacle, it is not surprising that the initial target for using HP gas MRI was the pulmonary system. The first demonstration was in an excised mouse lung (10). Hyperpolarized ^{129}Xe was introduced via the trachea and imaging followed immediately. This initial effort showed very little structure. Soon thereafter, two-dimensional (2D) and three-dimensional (3D) MRI of the lungs with HP ^{3}He were shown in dead guinea pigs (Fig. 1a) (11). Subsequently, imaging in live animals was accomplished with both isotopes (13–15). Noble gas MRI research moved rapidly from animals into human volunteers (16–18) and, finally, patients (19).

Biomedical HP gas MRI has been recently reviewed in two articles presenting a more hands-on implementation of lung MRI with ^{3}He (20) and summarizing initial clinical applications (21). In the present report, we seek to present
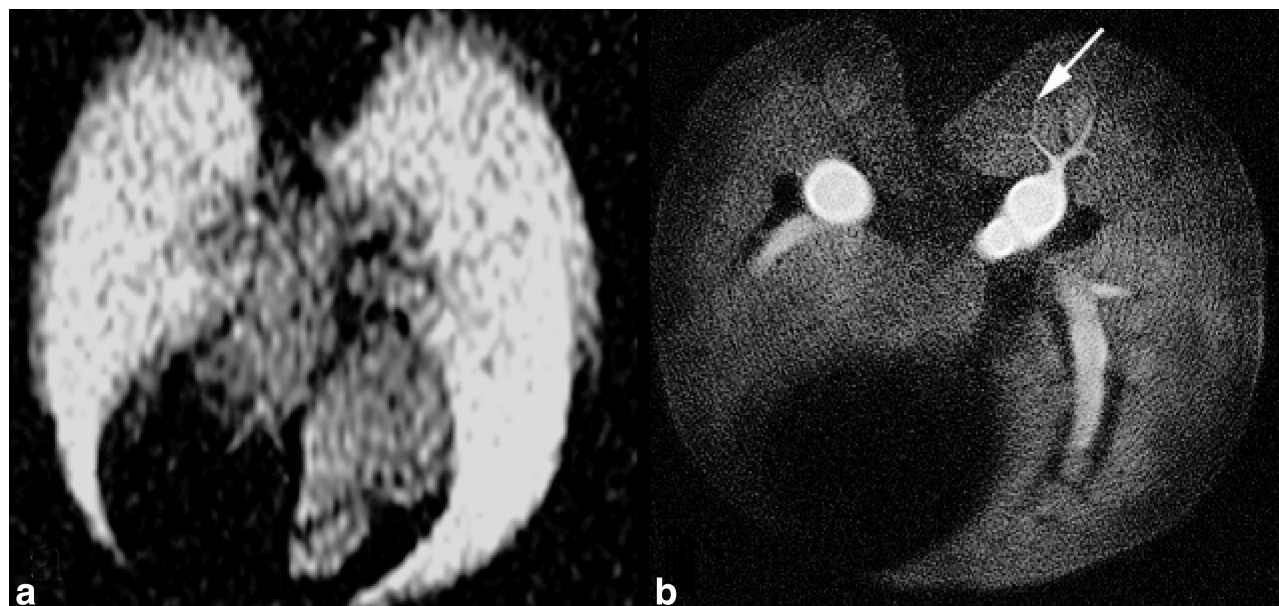
FIG. 1. Comparison of (**a**) the first HP ^{3}He lung image (axial orientation) ever recorded in a dead guinea pig (reproduced with permission from Middleton et al., Magn Reson Med 1995;33:271–275, © Wiley-Liss, Inc.), and (**b**) a high-resolution image obtained in a live rat using currently available technology (12). The diameter of the small airway indicated by the arrow is estimated to be ~100 μm.

a more general but comprehensive picture of the field as it has developed in the last several years. One focus is the underlying physics enabling the use of HP gases in MRI, the technologies for OP, and some aspects of imaging strategies that effectively use the hyperpolarization. In any MRI experiment, the signal reflects a number of different physical parameters, such as spin density, relaxation times, and molecular mobility. Understanding the effects of tissue microstructure on relaxation and the apparent diffusion coefficient (ADC) is therefore another goal. Exploiting such parameters for generating contrast further enhances information obtained about morphology and function. Finally, recent applications of HP gas MRI to the healthy and diseased lung of animals and patients are summarized.

OPTICAL PUMPING

Hyperpolarized gas is produced through the transfer of angular momentum from circularly polarized light to the noble gas nucleus. Each photon carries $+\hbar$ or $-\hbar$ of angular momentum along the axis of its propagation. One of two basic methods is usually employed: 1) spin exchange with an optically pumped alkali-metal vapor (usually Rb, although K and Cs can also be used), or 2) direct OP of metastable ^{3}He. A third method is under development (22,23), whereby the gas is produced thermally via "brute force" at $B_0 \geq 10T$ and $T < 10$ mK. In both optical schemes the transfer of angular momentum occurs in two stages: first from light to electron spins and then from electron spins to the noble-gas nuclear spins. Spin-exchange optical pumping (SEOP) can be done with any nonzero-spin noble gas over a broad range of pressures (up to ~10 atm). Metastability exchange optical pumping (MEOP) is intrinsically much faster but can only be used with ^{3}He at

relatively low gas pressure (a few Torr). As HP gas production is light-limited for both techniques (more so for SEOP), the light source used is a laser, tuned to the appropriate atomic transition frequency, incident on a 50–200 cm^3 valved glass vessel ("cell") containing the noble gas. In the case of SEOP, the cell also contains a small quantity of nitrogen gas and a visible quantity of the alkali metal (a few hundred milligrams). The present discussion deals primarily with ^{3}He, which has the most widespread use in MRI. The only other noble-gas isotope widely studied and used is ^{129}Xe. These two stable spin-1/2 isotopes are favored because the absence of intraatomic quadrupole interactions leads to longer relaxation times.

Spin-Exchange Optical Pumping of ^{3}He

A review of SEOP has been given recently by Walker and Happer (24); we will briefly discuss the applicable points. In SEOP, the laser light is incident on a vapor of alkali-metal atoms in the cell. The valence electron of the alkali metal is polarized by the light to nearly 100% by depopulation OP (25), a process depicted in Fig. 2. The light excites the principal electric dipole (D_1) transition, $ns_{1/2} \rightarrow np_{1/2}$, of the valence electron. Here, n is the principal quantum number ($n = 5$ for Rb); s and p indicate the orbital angular momentum quantum numbers of 0 and 1, respectively, and the subscript 1/2 refers to the total (orbital plus spin) angular momentum quantum number j for both states. The wavelength of this light for rubidium is 794.8 nm. The ground and first excited states each have two sublevels corresponding to the magnetic quantum numbers $m_j = \pm 1/2$.

The use of circularly polarized light with either negative (σ^-) or positive (σ^+) helicity imposes an additional selection rule for absorption of electric dipole radiation. Using
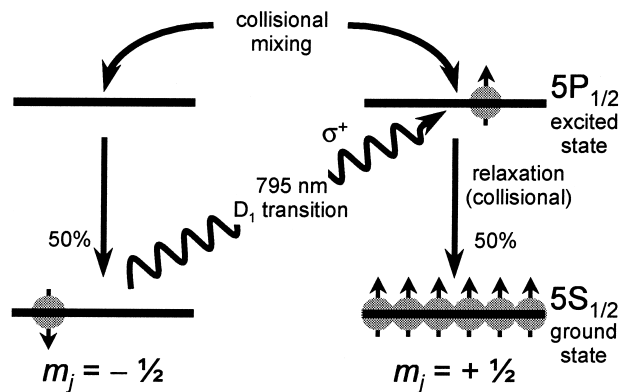
FIG. 2. Schematic representation of depopulation OP in Rb. The $5S_{1/2}$ and $5P_{1/2}$ states are each split into two magnetic sublevels. Right-handed circularly polarized laser light (σ^+) can only excite the transition indicated by the wavy line, depopulating the spin-down sublevel of the ground state. The optically excited atoms have their electron polarization nearly completely destroyed by binary collisions (collisional mixing) with the high-pressure buffer gas (i.e., ^{3}He/N$_2$ and Xe/^{4}He/N$_2$ mixtures in case of ^{3}He and ^{129}Xe SEOP, respectively) before they repopulate both ground state sublevels with equal probability by quenching collisions with N$_2$. Once in the $m_j = +1/2$ ground state, the atoms cannot absorb the laser light.

the example of σ^+ light, a transition may only proceed from the $-1/2$ ground-state sublevel to the $+1/2$ excited-state sublevel, conserving the $+\hbar$ of angular momentum carried by the photon. The atoms spend very little time in the excited state relative to the photon-absorption time, decaying to the ground state in times of order 10^{-9} sec. Prior to decay, rapid collisions with ^{3}He atoms in the high-pressure gas phase nearly completely destroy the electron spin polarization. Due to this collisional mixing of the excited-state sublevels (26,27), both ground-state sublevels are repopulated with equal probability. The small amount of N$_2$ (~ 0.1 atm) causes the decay to occur collisionally without the emission of a photon. This is important for efficient OP, since emitted photons can have the wrong helicity and be reabsorbed by the vapor ("radiation trapping"). Because only one ground-state sublevel can absorb light, nearly all of the electrons land and eventually are stuck in the nonabsorbing sublevel, thus polarizing the alkali-metal vapor. Other processes that tend to destroy electronic polarization (28) work on 1–10 ms timescales, much longer than typical OP time scales of tens of microseconds. Hence, alkali-metal polarizations approaching 100% are feasible.

The second stage of SEOP occurs in collisions between the polarized alkali-metal atoms and the ^{3}He atoms. During the collision, a Fermi contact interaction of the form a **I** $\cdot$ **S** occurs between the alkali-metal electron (spin **S**) and the ^{3}He nucleus (spin **I**), where a is a coupling-strength parameter. This interaction is due to the overlap of the valence electron wavefunction with the ^{3}He nucleus during a collision. The energy difference involved with simultaneously flipping an electronic and a nuclear moment is taken up by a change in the collisional kinetic energy. After the collision, the alkali-metal atom is restored to its previous spin orientation by continued OP, ready to collide with another ^{3}He atom.

The ^{3}He nuclear polarization grows exponentially as a function of time:

$$P_N(t) = \langle P_A \rangle \frac{\Gamma_{se}}{\Gamma_{se} + R_1} \{1 - \exp[-(\Gamma_{se} + R_1)t]\}, \quad [3]$$

where $R_1 = 1/T_1$ is the ^{3}He longitudinal relaxation rate in the absence of any Rb, and $\langle P_A \rangle$ is the alkali-metal electron spin polarization, time- and volume-averaged across the OP cell. The spin-exchange rate, Γ_{se}, is directly proportional to the alkali-metal number density, [A]. As $t \to \infty$, $P_N \to \langle P_A \rangle$ provided $\Gamma_{se} \gg R_1$. For Rb, temperatures between 170 and 200°C are typically required to create a sufficiently dense vapor. Changing the cell temperature can be used to adjust [A] and Γ_{se} can thus be made as large as desired; however, if [A] becomes too large, $\langle P_A \rangle$ cannot be maintained at close to 100% due to lack of sufficient laser power. Consequently, SEOP involves a balance between maximizing Γ_{se} to achieve maximum polarization in a reasonable amount of time and maintaining $\langle P_A \rangle$ near 100% with a fixed available amount of laser light.

As practically implemented, SEOP takes place in a small (1–3 mT) applied magnetic field, which must be collinear with the direction of propagation of the laser light. The field allows NMR detection at ~ 100 kHz to monitor the generation and decay of noble-gas polarization; it also allows the entire apparatus to be located independently of the local direction of Earth's field (~ 0.05 mT); and it helps to inhibit gradient-induced spin relaxation due to diffusion (29,30). The last 10 years have seen the development of inexpensive laser-diode arrays (LDAs; e.g., Coherent Semiconductor Group, Santa Clara, CA) capable of $10-100$ W of power, which are now routinely used. These lasers, in particular, have made feasible the production of liter quantities of HP gas in several hours by SEOP. A drawback is their very large frequency width, typically 1–3 nm, very much broader than typical atomic transitions. The width necessitates working at high ^{3}He pressures ($p \approx 8-10$ atm), which sufficiently broadens the Rb D$_1$ transition line, allowing a larger fraction of the available laser light to be absorbed.

In general, it is possible to orient the noble-gas spins in either the high- or low-energy nuclear Zeeman state. This can be accomplished by reversing the helicity of the OP light with respect to the direction of the applied magnetic field. For MRI, the low-energy orientation is strongly favored: in the high-energy state, highly polarized spins can undergo stimulated emission (masing) in a suitably high-Q resonant-circuit probe (31), destroying the magnetization. Since both ^{3}He and ^{129}Xe have their magnetic moments opposite to their spin, the light helicity and magnetic field should point in opposite directions.

Metastability-Exchange Optical Pumping of ^{3}He

Originally, MEOP was developed at about the same time as SEOP (32). Two more recent articles (33,34), while not exhaustive, discuss technical developments and point to progress made in the field over the last 40 years. As with spin exchange, MEOP uses a polarized electron state to polarize the ^{3}He nucleus. The key difference from SEOP is that the electron-nuclear coupling takes place entirely

Table 1
Physical Properties of the Noble Gas Isotopes ^{3}He and ^{129}Xe

Parameter	^{3}He	^{129}Xe	Ref.
Nuclear spin, I	1/2	1/2	39
Magnetogyric ratio, γ (10^7 rad s^{-1} T^{-1})	−20.3781587	−7.452103	39
Natural abundance (%)	1.37×10^{-4}	26.4	39
Chemical shift range,[a] $\Delta\delta$ (ppm)	~0.8	~250	40, 41
Spin-lattice relaxation time,[b] T_1 (h)	744	55	42, 43
O_2-dependent relaxivity,[c] κ (s^{-1} Pa^{-1})	3.85×10^{-6}	3.73×10^{-6}	44, 45
Self-diffusion coefficient, D_0 (cm^2 s^{-1})	2.05	0.061	46
Diffusion coefficient in air,[d,e] D (cm^2 s^{-1})	0.86	0.14	46
Ostwald solubility in blood,[d] L	0.0085	0.17	47

[a]Gas-to-solution solvent shifts of ^{3}He and ^{129}Xe dissolved in common liquids.
[b]Pure gas at room temperature and atmospheric pressure.
[c]Noble gas/O_2 mixture at body temperature.
[d]At body temperature and atmospheric pressure.
[e]Approximating air as a mixture of 79% N_2 and 21% O_2.

within a given ^{3}He atom without the need of an intermediary alkali metal. The electron polarization is accomplished by first populating the metastable $^3S_1$ state of helium with a weak RF discharge at $p \approx 1$–10 Torr. Optical pumping proceeds using the transition at 1083 nm connecting the $^3S_1$ to the $^3P_0$ state, depopulating certain spin sublevels in the metastable state in a fashion similar to that described for SEOP. Once the electrons are polarized, the strong intraatomic hyperfine coupling assures very rapid polarization of the ^{3}He nucleus.

The second stage of angular momentum transfer in MEOP occurs during collisions between the polarized metastables and unpolarized atoms in the ground state. During the collision the two species essentially exchange electron states (32,33) without affecting the nucleus of either atom. Thus, the new ground-state atom keeps its oriented nucleus, leaving the new metastable atom to be polarized by the laser.

As practically implemented, the low pressures mean that the ^{3}He in MEOP is optically thin, requiring long, narrow OP cells in order to make the best use of the laser light. With the aid of partial mirrors at the ends the light passes several times through one or more such cells. Although diode lasers have been used as a source of the 1083-nm light (34), the best results are still obtained with an arc-lamp-pumped, neodymium-doped lanthanum magnesium hexaluminate (LMA) laser (33), which is made by replacing the gain medium in a commercial Nd:YAG laser. The cell is part of a flow-through arrangement in which the ^{3}He gas, once polarized, must be compressed by a factor of ~100 to reach atmospheric pressure. The state-of-the-art MEOP system was developed at the University of Mainz (35,36). This system uses four 1-m long cells, an LMA laser, and a piston compressor made mostly of titanium to inhibit ^{3}He relaxation.

The main advantage of MEOP is its much higher intrinsic polarization rate. The photon efficiency is typically at or near unity, as compared to about 0.05 for Rb-^{3}He SEOP (28). The characteristic time for polarizing ^{3}He is thus usually measured in tens of seconds vs. several hours for SEOP. This advantage has to be balanced against the need to compress the gas without losing polarization, a more costly laser, and a larger, less portable system overall.

Developments in both fields may impact this picture in the near future. More compact systems for polarizing and compressing ^{3}He by MEOP based on a peristaltic pump (37) or a modified commercial diaphragm pump (38) have been demonstrated. On the SEOP side, Ben-Amar Baranga et al. (28) measured photon efficiencies in the K-^{3}He system that are about an order of magnitude higher than for Rb-^{3}He and 15-W LDAs have been developed at the D_1-transition wavelength (769.9 nm) for potassium.

Wall Relaxation

A crucial issue in HP gas production is longitudinal relaxation of the noble-gas spins in the OP and storage cells. This relaxation has two important consequences: 1) it limits the ultimate achievable polarization P_N (see Eq. [3]), and 2) it limits storage time of HP gas. The dominant process is usually due to interactions occurring at or near the surface of the cell ("wall relaxation"), with some contribution at higher pressures coming from the bulk dipole–dipole interaction between noble gas spins (Table 1). A third mechanism, gradient-induced relaxation by diffusion of the noble gas (29), is usually made negligible by the use of a suitably uniform applied field, such as from a Helmholtz-coil pair. While the subject of a great deal of research over the last few decades, wall relaxation of noble gas nuclei to most surfaces is still only poorly understood. What has emerged is a wide variety of recipes and protocols for glass type, surface preparation or coating, alkali-metal distillation procedures, and other aspects of cell fabrication. The results have been mixed, often irreproducible, and usually specific to one research group or to certain equipment.

In SEOP, since characteristic spin-exchange times, $1/\Gamma_{se}$, are at least several hours, T_1s of tens of hours in the OP cell are required to build up appreciable polarization. Early research suggested that the large He permeability in borosilicate glasses such as Corning 7740 (Pyrex) made these glasses a poor choice for cell fabrication (48). Aluminosilicate glasses (42,48,49) have been used with some success, although these glasses are not as readily available, are more expensive, and are difficult for glass blowers to work. In addition, scaling up cells made from the aluminosili-

cates to the large sizes needed for MRI has proven problematic. Pyrex remains a desirable choice because it is rugged, inexpensive, and easy to work. Recently, wall relaxation times of many tens of hours were observed in Pyrex cells (20,50), suggesting that this glass be reexamined for use in HP gas production.

For MEOP, the situation boils down to the relaxation characteristics of the surfaces in the compression system and in the storage cells. The rapid intrinsic polarization rate usually means that the OP cell itself need not be optimal. Storage cells with T_1s in the hundreds of hours have been made using iron-free aluminosilicate glasses (51), or by coating the interior surface with a macroscopic metallic layer of rubidium or cesium metal (52). Such metallic coatings cannot be used for SEOP cells since the Rb and Cs bead into a puddle at the bottom of the cell as soon as it is heated for OP.

Polarizing ^{129}Xe

To polarize ^{129}Xe, SEOP can be used in much the same way as outlined above for ^{3}He, but there are important differences. The characteristic spin-exchange time is tens of seconds or a few minutes for Rb-^{129}Xe as compared to hours for Rb-^{3}He (53); the spin-exchange interaction is much stronger for ^{129}Xe because of the enhanced attraction of the Rb valence electron to its 54 protons. Unfortunately, xenon has large adsorption energies (of order 0.1 eV) on most surfaces (including glasses), so that wall relaxation times are tens of minutes to a few hours at most (54). In addition, OP efficiency is much worse for Rb-^{129}Xe because of the large spin-rotation interaction (55). As seen by the Rb atom, the Xe electrons generate magnetic fields during the collision, which depolarize the Rb electron. It is difficult to polarize ^{129}Xe in "batch mode"—at pressures of 8–10 atm—as is commonly done with ^{3}He. The depolarization rate due to spin-rotation depends linearly on Xe density and typically limits the cell pressure to 2–3 atm. Typical temperatures of 95°C were found to achieve an optimum Rb vapor density under such conditions. The lower pressure also reduces the number of photons absorbed from the LDA, since the pressure broadening of the D_1 transition is proportionally reduced. Despite these limitations, Rosen et al. (56) achieved $P_N \approx 7.5\%$ in 150 atm cm^3 batches of naturally abundant Xe with a 15-W LDA.

Another approach, first taken by Driehuys et al. (57), uses a lean mixture of 1–2% Xe and 1% N$_2$, with the balance being ^{4}He. The high-pressure (~10 atm) ^{4}He broadens the D_1 line without introducing a strong spin–rotation interaction. Typically, the polarizing chamber is maintained at temperatures between 130–150°C to achieve 60% laser absorption. The ^{129}Xe is polarized in a flow-through system and then separated cryogenically from the other gases. At $T = 77$ K and $B_0 > 0.05$ T, $T_1 \approx 2.5$ h for solid ^{129}Xe (58). The polarized ^{129}Xe may then be accumulated in the solid state for times of order T_1 and then sublimed after residual gases have been pumped away. With the available lasers, accumulation schemes should in theory produce ~1 L/h (standard temperature and pressure) of 70–80% polarized ^{129}Xe gas. In practice, these schemes have been limited by losses incurred while gas flows into the cryogenic trap and during the freezing and thawing processes. Polarizations reported in the literature using accumulation schemes still do not exceed 15–20%.

COMPARISON OF ^{3}HE AND ^{129}XE FOR USE IN LUNG MRI

Current experimental evidence indicates an enormous potential of both ^{3}He and ^{129}Xe for various aspects of pulmonary imaging. Physical properties of the two isotopes are summarized in Table 1. Several practical advantages suggest that ^{3}He may be regarded superior for direct visualization of gas-space morphology. Its magnetogyric ratio—and hence the magnetic moment—is 2.7 times larger than for ^{129}Xe, which translates directly into a sensitivity advantage (see below) under otherwise equivalent experimental conditions. Despite the negligible natural abundance of ^{3}He, sufficient supply at a cost of ~$100/L is currently available from its production through the nuclear decay of tritium. Natural Xe gas, which is recovered from the atmosphere, costs ~$20/L, whereas gas enriched to higher concentrations of ^{129}Xe is significantly more expensive (~$700/L for enrichment to 80% ^{129}Xe). In principle, both gases should be recyclable after use for imaging but so far this has not been put into practice. Due the high cost of working with enriched ^{129}Xe, an additional SNR advantage for ^{3}He by a factor of 3.8 results from the isotopic composition of the polarized gas (i.e., pure ^{3}He vs. naturally abundant ^{129}Xe) normally used in HP gas MRI. As discussed above, liter quantities of both gases can now be routinely produced with polarization levels of approximately 40% for ^{3}He and 20% for ^{129}Xe, which further contributes to the sensitivity advantage of ^{3}He MRI. In summary, we may expect that the SNR of typical ^{3}He lung images exceeds that achieved with ^{129}Xe MRI by an order of magnitude, consistent with experimental results from a thorough comparison of both nuclei (59). Furthermore, He/O$_2$ mixtures can be breathed indefinitely (e.g., by deep-sea divers), whereas Xe is a general anesthetic (60) in high concentrations (>70%). However, ^{129}Xe has unique characteristics (e.g., solubility in blood and tissues, smaller diffusivity, wide range of chemical shifts), which may be exploited for selected applications (e.g., perfusion imaging) as discussed in more detail below.

IMAGING UNDER NONEQUILIBRIUM CONDITIONS

Conventional MRI sequences are usually based on the fact that the polarization state is initially in equilibrium and will recover after RF pulsing. Since HP gas is far from an equilibrium state, certain aspects of our imaging procedures must be adapted accordingly.

Disregarding contributions from the MR apparatus, the NMR signal level from HP gas with nuclear spin 1/2 is:

$$S_{HP} = \frac{1}{2} N |\gamma| \hbar \omega_0 P_N, \qquad [4]$$

where P_N is on the order of 10^{-1} and field independent. $\omega_0 = \gamma B_0$ is the Larmor frequency. The signal at thermal equilibrium exploited for conventional MRI is:

$$S_0 = \frac{1}{2} N|\gamma|\hbar\omega_0 P_{N,0} = \frac{N|\gamma|\hbar^2\omega_0^2}{4k_B T}, \qquad [5]$$

with the equilibrium polarization given by Eq. [2] (typically on an order of 10^{-6}). Experience shows that for frequencies $\omega_0/2\pi$ above a few MHz inductive losses in the sample are the dominant noise source in biological tissues and the root mean square of the noise voltage is proportional to ω_0 (61). Under such conditions, the SNR is independent of ω_0 in HP gas experiments instead of the linear frequency dependence found in conventional MRI. As there is no sensitivity gain from increasing B_0 in this regime, low-field systems are attractive for use in HP gas MRI (62,63). At sufficiently low fields or for sufficiently small samples (e.g., in small-animal studies), however, losses of the receiving coil (i.e., Johnson noise) dominate over the "tissue noise" unless the coil is cooled. Due to the RF skin depth of the coil, Johnson noise shows a weak dependence on the NMR frequency ($\sim\omega_0^{1/4}$), and the HP gas SNR begins to scale with $\omega_0^{3/4}$. A possibly optimum operating frequency for HP gas experiments might therefore be defined by the limit where inductive tissue losses are reduced to the level of losses of the receiving coil.

Any deviation of the longitudinal magnetization, M_z, from its Boltzmann equilibrium value, M_0, is followed by thermally driven relaxation. Therefore, T_1 is conventionally considered as the time constant for M_z to recover after application of an RF pulse. However, because HP gas MRI is conducted far from equilibrium, M_z typically exceeds M_0 by a factor of 10^4–10^5, and longitudinal relaxation is well approximated by:

$$\frac{dM_z}{dt} = -\frac{1}{T_1}(M_z - M_0) \approx -\frac{1}{T_1}M_z. \qquad [6]$$

Equation [6] demonstrates that hyperpolarization never recovers once the laser is turned off, but continuously decays towards an unmeasurably small equilibrium value. In addition, every excitation of the spin system with an RF pulse of flip angle α uses up a fraction $(1 - \cos \alpha)$ of the polarization. As a consequence, automated routine procedures for adjusting frequency, transmitter, and receiver-gain settings must be avoided because they cause unaffordable loss of hyperpolarization. Alternatively, frequency and flip angle adjustments can be performed using glass cells containing thermally polarized ^{3}He/O$_2$ or ^{129}Xe/O$_2$ mixtures at elevated pressure. The presence of O$_2$ reduces T_1 from several hours to a few seconds (44).

Experiments with noble gases may be performed on ordinary MR scanners provided that broadband RF transmit/receive hardware is available, which can adjust to the respective Larmor frequencies of ^{3}He ($\sim\frac{3}{4}$ of the ^{1}H frequency) or ^{129}Xe ($\sim$10% greater than the ^{13}C frequency). Typically, imaging coils have been built in-house, although some companies have provided coils (e.g., IGC-Medical Advances, Milwaukee, WI or Fraunhofer Institute for Biomedical Engineering, St. Ingbert, Germany). Volume coils of birdcage design have yielded excellent results in small animals with HP ^{3}He (12,13,64) and ^{129}Xe (59,65). Suitable RF coils used in human investigations were in transmit/receive surface (17) or Helmholtz (19,66–68)

configurations. Such designs provide sufficient sensitivity at the expense of some nonuniformity of the signal, which typically falls off in depth. Improved homogeneity has been obtained with dedicated quadrature chest coils (69,70).

Employing 90° RF pulses in imaging sequences that require multiple repetitions to acquire all lines in k-space won't work because there will not be any residual z-magnetization after the first excitation (view). Most investigators have used strategies that sample the signal with small flip angles. Because there is no recovery, the repetition time, TR, can be made as short as possible, thus shortening scan times relative to proton lung scans. Ninety-degree pulses can be used in single-shot imaging sequences such as EPI (echo-planar imaging (71)) and spiral (72) (see below).

Both Fourier imaging with gradient-recalled echoes (GRE), such as FLASH (fast low-angle shot (73)), and projection reconstruction (PR) with radial encoding (1), have been employed experimentally (10,11,13) and evaluated theoretically (59,74). The quasi-periodic arrangement of air/tissue interfaces inside the lungs produces substantial variations of the bulk magnetic susceptibility (BMS) on a microscopic scale, which results in fast T_2^* relaxation (see below) and, thus, a short-lived NMR signal. As an advantage for imaging short-T_2^* species, PR permits capturing the signal as a free induction decay (FID) with an ultra-short delay time ($<$300 μs (75,76)). However, data sampling on a polar raster requires π times the number of views compared with Cartesian sampling.

Initial efforts in HP gas MRI were focused on visualizing gas in the lungs during inspiratory breathhold as it was both conceptually and practically simple. An example recorded in a normal human volunteer with ^{3}He is shown in Fig. 3. Such images are termed "gas density" because no special weightings or breathing techniques are used and the airways and alveolar airspaces were easily visualized (13–19,77). If multiple excitations at constant α are used to sample k-space data during breathhold periods, the signal contribution from the nth view is given by (78):

$$S(n) = M_z(0)\exp[-(n-1)TR/T_1]\cos^{n-1}\alpha \sin\alpha. \qquad [7]$$

As T_1 is usually long (i.e., $TR \ll T_1$), spin-lattice relaxation can be neglected in most cases. Optimizing the flip angle involves a trade-off between generation of transverse magnetization (i.e., maximizing $\sin \alpha$) and the rationing of nonrecoverable longitudinal magnetization, given by $M_z(0) \cos^{n-1}\alpha$. Appropriate solutions for α_{opt} as a function of the number of views, N_v, were published for both Fourier imaging (74) and PR (59). While the SNR would increase as $\sqrt{N_v}$ in conventional MRI, the usable magnetization is fixed in an HP gas experiment (i.e., independent of the number of encoding steps); hence, the SNR approaches an asymptotic level, as shown in Fig. 4. Another consequence from the nonequilibrium situation, which is inherent in the term $\exp[-(n-1)TR/T_1] \cos^{n-1}\alpha$ in Eq. [7], is a steady depletion of the signal level over the course of raw data sampling (64,78,79). This imposes a k-space filter, which may produce artifacts and results in suboptimal signal utilization (80,81). With typical flip angles $\alpha < 10°$,

FIG. 3. Coronal HP ^{3}He image of the lungs of a normal healthy human volunteer showing homogeneous distribution of signal throughout the pulmonary gas space. Secondary branching of the bronchi is visible as well as some pulmonary vasculature delineated as low-intensity structures.
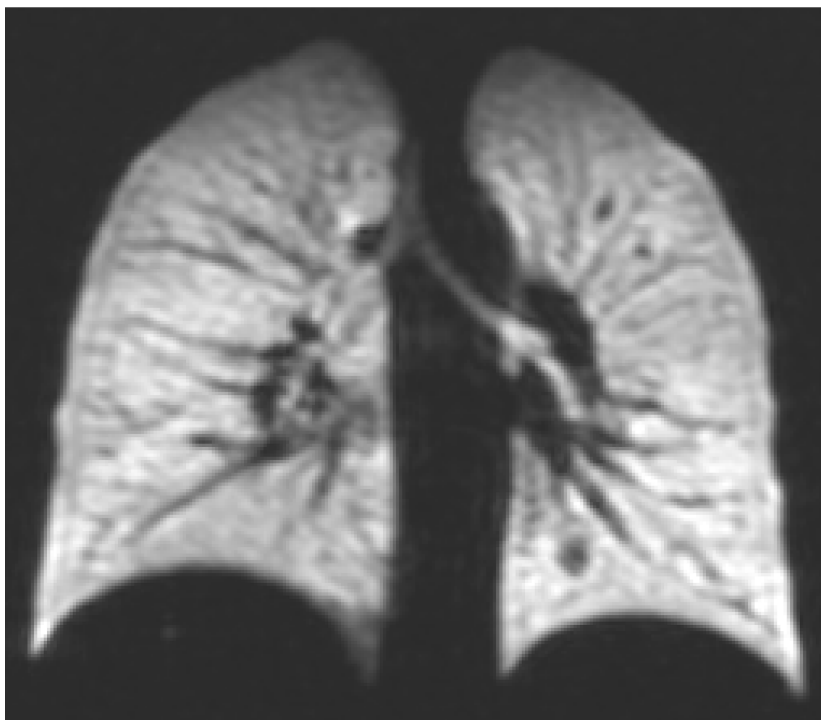
net signal changes are small, yielding a well-behaved k-space filter. As an alternative approach, the use of variable flip angle excitations to obtain uniform k-space weighting has been suggested (82,83). This strategy, however, is sensitive to flip-angle errors (74).

Another unique aspect of HP gas MRI is the ability to directly image the flow of gas into the lung. Johnson et al. (64) illustrated dynamic imaging in guinea pigs by sampling the magnetization over the entire breath. A large flip angle of 40° destroyed magnetization early in the inspiratory phase, highlighting the large airways. Gas was reaching the distal spaces, but all the signal had been destroyed by RF pulsing. Flip angles of 20° and 30° allowed magnetization to reach the distal airspaces. With the ability to produce more polarized gas, smaller segments of the breathing cycle were sampled (100 ms out of a 1500-ms breath), resulting in 5th generation airways being resolved (79). A model of the signal dynamics taking into account the magnetization, breathing cycle, and RF excitation has been developed and verified with experiment (78). Single-shot techniques, such as RARE (rapid acquisition with relaxation enhancement (84)), EPI, or PR with spiral k-space trajectories have also been implemented successfully (67,85–87). While EPI and spiral scanning provide excellent temporal resolution, they may be limited by the relatively rapid transverse decay rate inside the lungs (see below). Alternatively, interleaved EPI, spiral, and cylindrical techniques have been employed to improve spatial resolution (85,88,89).

While delivery of HP gas can be synchronized manually with imaging in human investigations, mechanical ventilation is often necessary for MRI of animals to maintain gas exchange, control breathing motion, and to deliver anesthetics and HP gas. Due to the relatively short breathing cycle in small animals, multiple breaths of HP gas may be required to accumulate sufficient raw data. Sophisticated ventilators that are compatible with MR scanners and deliver HP gas in synchrony with the imaging process and with minimum dead volumes have been described. For short scan times in normal animals, it is effective to use breaths of 100% HP gas alternated with breaths of air (90,91). For longer durations that are needed for scans on the order of hours—such as those required for 3D MR microscopy—simultaneously delivering O_2 and HP gas is physiologically more appropriate (92). Alternatively, a well-defined, small bolus of HP gas may be delivered at a predefined position within the tidal volume (93).

NOBLE GAS RELAXATION IN THE LUNGS

In addition to being in a nonequilibrium state, HP gas will relax differently than protons in a biological environment. The physical basis behind basic parameters like T_1, T_2, and T_2^* will stem from different sources as compared to protons, and it is crucial to obtain these measures to optimize pulse sequences and learn of potential contrast mechanisms.

Longitudinal Relaxation

Inversion-recovery (94), traditionally the workhorse for measuring T_1, is not applicable in HP gas experiments because the hyperpolarization does not recover after an inversion pulse. As a simple alternative, a periodic train of monitoring RF pulses of limited α, originally introduced by Look and Locker (95), proved to be a robust technique to determine HP gas T_1 in vivo (14,66,78). To obtain regional relaxation data, an equivalent approach has been exploited by using a series of fast GRE images (70,93) or single-shot spiral PR techniques (96).
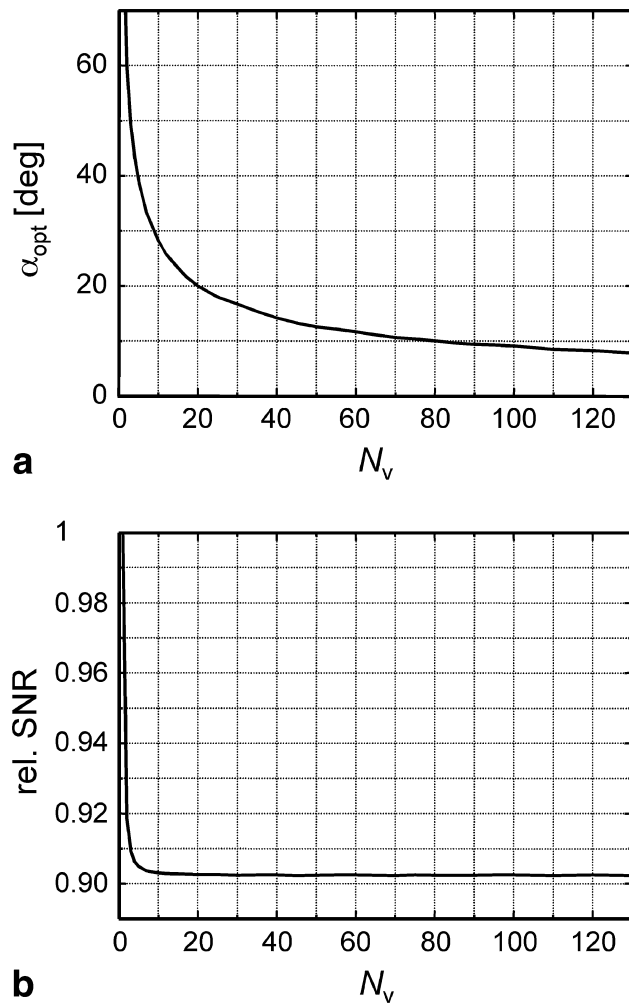
FIG. 4. Evaluation of HP gas MRI of the lung at breathhold using radial PR with N_v excitations at a constant flip angle (59). **a:** Plot of the flip angle that generates maximum SNR as a function of N_v. As repetitive sampling of k-space lines causes nonrenewable depletion of longitudinal magnetization, α_{opt} becomes smaller with increasing N_v. **b:** Because the magnetization is fixed in a HP gas experiment, the relative image SNR obtained at the optimum flip angle is largely independent of N_v.

Inside the lungs, T_1 is reduced to seconds for both isotopes (14,66,70,78,92,93,96) caused primarily by interaction with paramagnetic molecular oxygen, which leads to a linear relation between the noble gas relaxation rate and the O_2 partial pressure (Fig. 5):

$$1/T_1 = \kappa p_{O2}. \qquad [8]$$

At body temperature and typical fields of clinical scanners, relaxivities $\kappa = 3.85 \times 10^{-6}$ s^{-1} Pa^{-1} for ^{3}He (44) and $\kappa = 3.73 \times 10^{-6}$ s^{-1} Pa^{-1} for ^{129}Xe (45) can be extracted from in vitro studies. Compared with this mechanism, other potential sources of ^{3}He spin-lattice relaxation, including magnetic field gradients (29,30) or alveolar surface interactions, do not significantly contribute to T_1 ($T_1 = 261$ sec was estimated for wall relaxation in the deoxygenized lung of a dead pig (70)). Regarding agreement between

preliminary T_1 measurements in guinea pigs (78) and estimates derived with Eq. [8], we may expect a similar condition to be valid for ^{129}Xe.

If the gas composition is constant over the observation period, M_z decays exponentially as a consequence of relaxation and repetitive RF pulse excitation. This was verified experimentally for a range of physiologically meaningful O_2 concentrations in postmortem investigations of the guinea pig lung (96). Similarly, image-based T_1 values from large alveolar regions in live pigs correlated well with calculations using Eq. [8] and the global end-expiratory p_{O2} derived from conventional respiratory gas analysis (93). Routinely, indirect estimates of global alveolar p_{O2}, which require model assumptions, are derived using the end-expiratory O_2 concentration at the mouth, which is compared to the p_{O2} of arterial and venous blood. By contrast, HP gas T_1 imaging holds the unique potential of measuring regional p_{O2} directly. As the intrapulmonary p_{O2} distribution is governed by local ventilation, perfusion, and O_2 uptake, this constitutes a new approach to lung function analysis.

In vivo, HP gas T_1 becomes a function of time because pulmonary gas exchange leads to a fall in alveolar p_{O2} (corresponding to a rise in T_1, see Eq. [8]) during breathhold. Consequently, nonexponential decay curves are obtained, which can be analyzed quantitatively to yield an initial partial pressure $p_{O2}(0)$ immediately after inspiration of the gas mixture and a decrease rate $|\dot{p}_{O2}|$ (96). Investigation of the temporal evolution of intrapulmonary p_{O2} during one breath is thus feasible from such data. Under normal conditions, binding of O_2 to hemoglobin constitutes the rate-limiting step of oxygen transfer from the alveoli into the red blood cells. Hence, O_2 uptake is primarily limited by the blood flow in the capillaries but not by diffusion effects. Consistently, the decrease of p_{O2} was linear during breathholds of up to 35 sec in both animals and humans (70,96,97), as expected for perfusion-limited O_2 uptake. Additionally, $p_{O2}(0)$ and the decrease rate $|\dot{p}_{O2}|$ were positively correlated in healthy human vol-
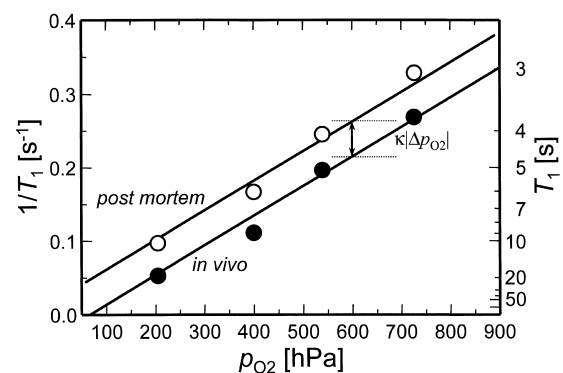

FIG. 5. ^{3}He spin-lattice relaxation rates $1/T_1$ inside the lung of a guinea pig measured in vivo (filled circles) and postmortem (open circles) as a function of the O_2 partial pressure in the inspired gas mixture. Due to pulmonary gas exchange, reduced alveolar p_{O2} is observed in the in vivo experiments as indicated by prolonged T_1. Solid lines show results from linear regression to Eq. [8]. The offset between both graphs corresponds to a difference in p_{O2} of ~64 hPa.

FIG. 6. Examples from a series of slice-selective in vivo HP ^{3}He images of the guinea pig lung recorded during breathhold at full inspiration (tidal volume 3 mL) with radial encoding and acquisition delays of (**a**) TE = 1 ms, (**b**) TE = 7 ms, and (**c**) TE = 15 ms. Signal loss with increasing TE is most prominent in regions near blood vessels (e.g., the parabronchial vessels). **d:** Calculated T_2^* map obtained from fitting of the pixel intensities of the images to an exponential decay. Reproduced with permission from Chen et al., Magn Reson Med 1999;42:729–737. © Wiley-Liss, Inc.
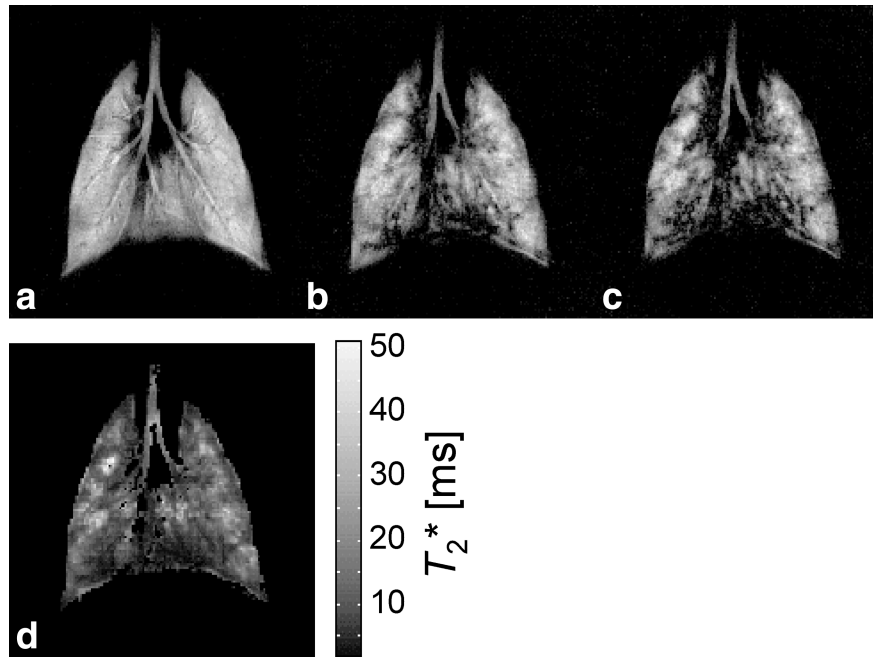
unteers, which points to local ventilation/perfusion ($\dot{V}/\dot{Q}$) matching (97). Via the Fick principle, alveolar p_{O2} is further related to quantities describing pulmonary function, such as the rate of O_2 uptake by the pulmonary circulation and the cardiac output. Estimations of such functional parameters from HP gas relaxation studies in guinea pigs agreed well with literature data (96). In another set of experiments, the functional residual capacity was obtained from spirometric relaxation measurements, in which HP gas T_1 was employed to probe the dilution of pulmonary O_2 after switching the composition of the breathing gas from a high to a low O_2 content (96). The results of 5–10 mL depending on the animal's body mass were within the normal range of literature data.

Most recently, the potential of HP ^{3}He T_1-weighted imaging for detecting perfusion abnormalities due to their effect on alveolar p_{O2} was demonstrated in an experimental pig model. After isolated pulmonary arterial occlusion using a balloon catheter, a focal T_1 reduction (i.e., corresponding to an abnormally high p_{O2}) was observed, which normalized upon deflation of the balloon (98).

Transverse Relaxation

In conventional proton MRI, most biological tissues are characterized by FIDs of durations of some hundred milliseconds. In contrast, lung has a much shorter FID due to bulk magnetic susceptibility (BMS) differences (99) at the air–tissue interfaces of alveoli and bronchioles (100,101). The fact that this signal loss (corresponding to inhomogeneous line broadening) arises from a mechanism internal to lung structure suggests that susceptibility effects contribute to the decay of the HP gas signal. The overall decay time, T_2^*, of the FID from the pulmonary gas space is therefore given by:

$$\frac{1}{T_2^*} = \frac{1}{T_2} + \frac{\gamma\delta B_0}{2} + \frac{1}{T_2'}, \qquad [9]$$

where δB_0 is the external magnetic field inhomogeneity and T_2' is the decay constant related to internal inhomogeneous broadening mechanisms, such as BMS effects.

A global measure of T_2^* may be obtained conveniently by recording the FID with variation of the acquisition delay (14,102). Spectra recorded in small animals demonstrated complex lineshapes, which are superpositions of peaks from different compartments, such as cylindrical and spherical structures that represent airways and alveoli. By extending the effective echo time, TE, in a GRE or radial PR sequence, T_2^*-weighted imaging is obtained. Animal and human studies were performed by Chen et al. (103) at magnetic field strengths of 2.0T and 1.5T, respectively. Inside the lung, T_2^* was in the tens of milliseconds, which is too short to be caused by field inhomogeneities of imaging magnets. It is expected that the pure spin–spin relaxation time, T_2, should be on the same order as T_1 inside the lungs (short correlation-time limit) because of the exceedingly short gas-phase collision-duration times (typically 10^{-13} sec). Experimentally, Darasse et al. (66) obtained T_2 = 8.9 sec from spectroscopic ^{3}He measurements in the human lung at 0.1T using a Carr-Purcell-Meiboom-Gill multiecho train (104,105), which agrees reasonably well with T_1. In summary, contributions to T_2^* from external inhomogeneities and T_2 processes are negligible, leading to the approximation $T_2^* \approx T_2'$. Hence, HP gas T_2^* is a parameter of the tissue microstructure.

In a series of spatially resolved in vivo measurements (B_0 = 2T) in guinea pig lungs at different states of inflation and levels of O_2, ^{3}He T_2^* was found to vary between 9 and 16 ms (Fig. 6), while 18.5 ms were obtained in experiments with ^{129}Xe (103). These values exceed proton T_2^* of lung tissue (101) by about a factor of 3 or more. In a human volunteer, the mean ^{3}He T_2^* was 9.4 ms at B_0 = 1.5T. Higher inflation volumes lead to increased T_2^*, indicating larger airspaces have a reduced BMS effect compared to smaller volumes. Transverse relaxation may be modeled quantitatively by treating the lung as a porous medium and
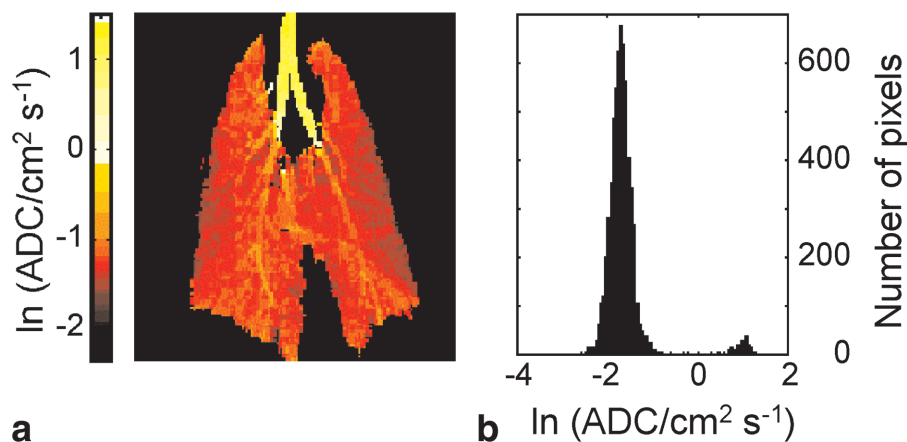
FIG. 7. **a:** Image of the ^{3}He ADC (logarithmic scale) in a live guinea pig lung, calculated from a series of nonslice-selective PR experiments with varying diffusion gradients (direction from top to bottom of the image; *b*-values between 0 and 5.8 s/cm^2). **b:** Corresponding histogram of ADC values. The diffusion coefficients from the extrapulmonary airways, which stand out as the brightest structures of the image, and from the darker-appearing pulmonary airspaces are distinctly separated into two peaks in the histogram. Reproduced with permission from Chen et al., Magn Reson Med 1999;42:721–728. © Wiley-Liss, Inc.

considering effects from restricted gas diffusion in a non-uniform magnetic field. Such models were described in detail by de Swiet and Sen (106) and Hürlimann (107). Briefly, BMS differences, $\Delta\chi$, cause a phase dispersion for spins precessing in the resultant nonuniform field. In the case of stationary nuclei, this decoherence leads to a T_2^* contribution that scales linearly with the inverse field variation, $(\Delta\chi B_0)^{-1}$. In a gas, the random walk of the diffusing nuclei motionally averages the phase dispersion—that is, the signal decay also depends on the diffusion properties. As a general finding, T_2^* varies as the square of the inverse field variation, $(\Delta\chi B_0)^{-2}$; hence, HP gas T_2^* may be substantially prolonged at low magnetic fields (63). In vivo T_2^* results obtained in guinea pigs were consistent with the assumption that diffusive motion averages out field inhomogeneities within individual pores, such as alveolar sacs (103). ^{3}He T_2^* in the lung measured at full inspiration increased with increasing tidal volume and decreased when alveolar p_{O2} was increased. Such responses are contrary to those observed in proton studies (108) because the spins of interest are in complementary compartments—that is, parenchyma vs. airspace.

DIFFUSION IN PULMONARY GAS SPACE

A unique difference between proton and HP gas MRI is the degree of diffusion. The water diffusion coefficient is on the order of 2×10^{-5} cm^2/s, which imposes a resolution limit of ~10 μm (109). By contrast, diffusion coefficients of gases are 10^3–10^5 times greater (Table 1). At first glance, these fast rates would appear to have a deleterious effect on the resolution. Fortuitously, two conditions in the lung significantly reduce the consequences from diffusion: 1) interactions of the noble gas atoms with lung gases, such as N$_2$ and O$_2$, and 2) restricted diffusion from the smaller length scales of the lung airspaces as compared to the diffusion length of the gas.

Measuring gas diffusion is equivalent to techniques used for ^{1}H NMR (104,110). During breathholds of HP gas, bipolar gradients are applied prior to signal acquisition to dephase and rephase spins (46,111–113). Spins that have diffused will contribute to signal attenuation; hence, the images will be weighted for diffusion. Unlike proton techniques, however, the "*b*-values" (related to bipolar gradi-

ent strength and duration) used are much smaller, typically 1–5 s/cm^2.

One factor that affects the gas transport properties is binary diffusion. Diffusion of a single type of gas in a free and isolated environment is denoted by the self-diffusion coefficient, D_0. Interactions of HP gas with unlike particles will change the mean free path of the noble gas atoms (and vice versa). The presence of a different type of gas will either reduce or increase the diffusivity, depending on the relative masses of the interacting gases. According to the theory developed by Chapman and Enskog in Ref. 114, the binary diffusion coefficient of ^{3}He in air is $D = 0.86$ cm^2/s (Table 1). This is reduced from $D_0 = 2.05$ cm^2/s due to ^{3}He collisions with the larger and heavier air particles. The binary diffusion coefficient of ^{129}Xe in air is 0.14 cm^2/s. In this instance, the N$_2$ and O$_2$ molecules are relatively smaller and lighter than the ^{129}Xe atoms, hence the increase from $D_0 = 0.061$ cm^2/s.

The second factor that changes the diffusivity is the airspace dimensions in relation to the diffusion length of the gas. The diffusion length, l_D, is the root-mean-square distance a particle travels for an observation time, *t*. For one dimension, the Einstein-Smoluchowski relation predicts $l_D = \sqrt{2Dt}$. Assuming binary diffusion and an observation time of 5 ms (i.e., a typical *TE* of an MRI sequence), l_D is 930 μm and 370 μm for ^{3}He and ^{129}Xe, respectively. As average diameters of the alveolar sacs are around 150 μm for small animals and 260 μm for humans (115), we are in the regime of restricted diffusion. Diffusion in restricted volumes may lead to image distortions, in particular edge enhancement (i.e., an artificially increased signal intensity near the impermeable sample boundaries), as suggested by theoretical analysis of the diffusion problem with boundary conditions (106,116). Experimentally, such effects were observed in phantoms of suitable size for both HP ^{3}He (113,117) and ^{129}Xe (118). More recently, Johnson et al. (12) demonstrated edge enhancement in a main stem bronchus of a live rat in 3D HP ^{3}He images.

The change in the ADC has been found experimentally in both animals and humans. Chen et al. (46) used multiple diffusion-weighted images to calculate ^{3}He and ^{129}Xe ADC maps of coronal projections as well as 5-mm thick

FIG. 8. Magnetic resonance $\dot{V}/\dot{Q}$ scan showing (**a**) normal ventilation on a HP ³He ventilation image and (**b**) a mismatched perfusion defect in the left lower lobe on a ¹H perfusion image. ¹H and ³He imaging were performed sequentially with coronal slice orientation in a rabbit model of pulmonary embolism. The location of the perfusion defect is indicated by an arrow. Reproduced with permission from Hagspiel et al., Eur Radiol 1999;9:B20. © Springer-Verlag GmbH & Co. KG.
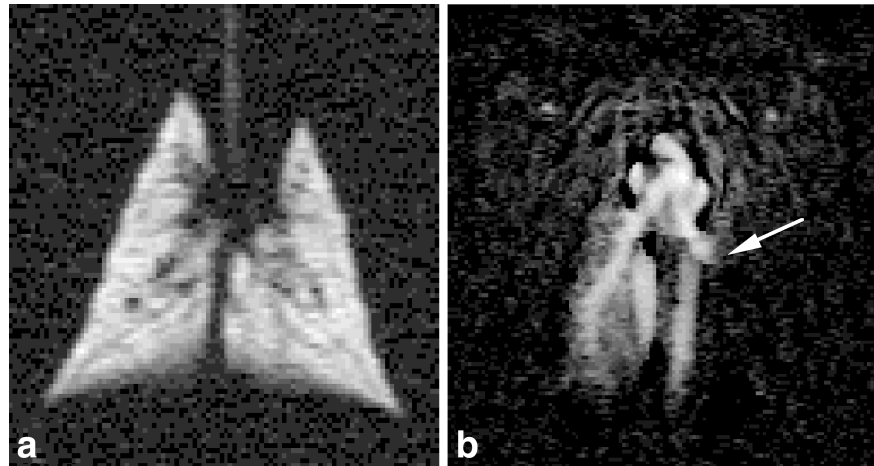
coronal slices in live guinea pigs (Fig. 7). In the clinical domain, ADC maps were calculated in volunteers, using a diffusion-weighted GRE sequence on 10-mm thick coronal slices (119,120). The average ³He ADC measured along the length of the trachea was 2.4 cm²/s in guinea pigs. In the human trachea (direction of the long axis), ADC values of 0.9–1.0 cm²/s were obtained (120). These numbers agree with the theoretical results (Table 1) for unbound ³He self-diffusion (small animal trachea) and binary diffusion of ³He in air (human trachea), respectively. The difference in the gas composition (pure ³He vs. ³He/air mixture) in the region of interest in the animal experiment may be explained by the different techniques used for gas delivery and the relatively smaller tidal volume as compared to the lung volume in the human study. The ³He ADC was reduced by about half in the transverse direction of the guinea pig trachea, indicating restricted diffusion (46). By contrast, isotropic diffusion in the trachea was observed for ¹²⁹Xe (ADC of 0.068 cm²/s), as the diffusion length is comparable to the width of the trachea in this case.

In healthy small-animal lungs, the average ³He ADC in the alveolar spaces was reduced by an order of magnitude to 0.10–0.34 cm²/s, depending on the state of inflation (46,121). The ¹²⁹Xe ADC was diminished by a factor of three to 0.021 cm²/s. There appeared to be no correlation between ADC and direction of sensitization. A diffusion study comparing healthy and asymptomatic, elastase-induced emphysematous rats indicated a significant increase by ~20% of the ADC at end-expiratory volume in the disease group (121). The increased ADC implies less restriction to diffusion, which is indicative of larger airspaces resulting from alveolar wall breakdown. Results were verified with histology. For human volunteers, the range of the ³He diffusion coefficients has been measured to be 0.17–0.40 cm²/s (119,120,122). As suggested by the results of the animal studies, noble gas diffusion imaging has already found application in patients with emphysema, which is discussed in more detail in the clinical imaging section (below).

A model developed for the study of gas kinetics in porous media (123) has been adapted to study the ADC reduction. The model states that the ADC is reduced from the free diffusion coefficient by a factor relating to the porosity and the tortuosity of the material. The porosity is defined as the ratio of the pore volume over the total volume. Tortuosity is a geometric property of a porous substance that characterizes fluid transport over long length and time scales (i.e., times much longer than it takes to cross a typical pore). Using reasonable estimates for both properties of the tissue, good agreement was found between experimental data as compared to theory (46). Further information may be obtained from time-dependent investigation of diffusion: For observation times t (defined by the time separation of the diffusion-encoding gradients) much less than the time for a spin to diffuse across a pore, ADC values close to those of the bulk gas are observed, whereas for longer t, the ADC decreases as the motion is increasingly restricted by the pore boundaries. Such experiments may ultimately yield characteristics of pulmonary microstructure and its fluid permeability, including the alveolar surface–area-to-volume ratio, average pore size, and tortuosity. Initial demonstrations of time-dependent ADC studies with HP ¹²⁹Xe in packed beads and oil-reservoir rocks (124,125) and, most recently, with HP ³He in human lungs (126) have been reported.

PULMONARY GAS EXCHANGE AND PERFUSION

Several groups have directed their efforts at developing the MR equivalent to the radionuclide $\dot{V}/\dot{Q}$ scan. This is of critical clinical importance for the assessment of a variety of lung disorders, such as pulmonary embolism. Although the radionuclide techniques are widely available, their limited spatial and temporal resolution is the main impetus for the development of new HP gas-based $\dot{V}/\dot{Q}$ techniques. Besides exploiting noble gas T_1 as a contrast parameter (see above), information on gas exchange and pulmonary perfusion may also be obtained from other experimental strategies.

³He Ventilation/¹H Perfusion MRI and ³He Ventilation/Perfusion MRI

Groups at the Universities of Lyon and Virginia demonstrated the feasibility of a combined ³He/¹H $\dot{V}/\dot{Q}$ MR scan in animal models of pulmonary embolism. Crémillieux et al. (127) utilized 3D PR for HP ³He ventilation MRI and Gd-enhanced ¹H perfusion imaging (128) of rat lungs. The
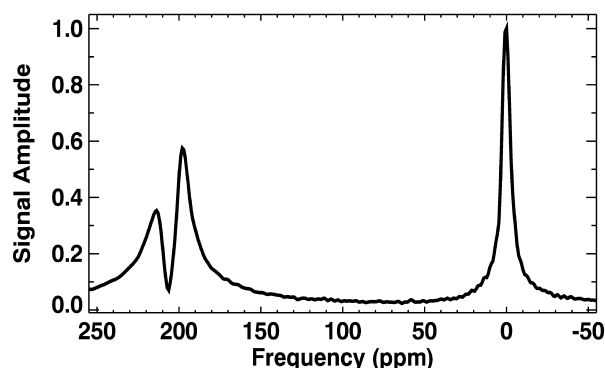
FIG. 9. Representative HP ^{129}Xe NMR spectrum from the dog chest acquired during breathhold. The signal at 0 ppm corresponds to gas in the lung while the peaks at 197 and 212 ppm arise from ^{129}Xe dissolved in the lung parenchyma and ^{129}Xe bound to hemoglobin, respectively. The pulse sequence utilized a Gaussian-shaped RF pulse (900-μs duration, flip angle 90°) centered at 202 ppm. As a consequence, the flip angle at the gas-phase resonance was less than 1°; hence, the peak at 0 ppm appears artificially small. Courtesy of Kai Ruppert, University of Virginia.

Virginia group (129) used ^{3}He density imaging and a method based on arterial ^{1}H spin tagging (130) for the diagnosis of embolism in rabbits after temporary balloon occlusion of the pulmonary artery. The combination of ^{3}He and ^{1}H MRI enabled the detection of pulmonary embolism as mismatched defects with perfusion deficit but normal ventilation, thus representing the equivalent to the nuclear medicine $\dot{V}/\dot{Q}$ scan (Fig. 8). ^{3}He ventilation MRI was also shown to allow detection of air leaks in animals (131). Researchers at the University of Pennsylvania (131–133) demonstrated the use of ^{3}H/^{1}H $\dot{V}/\dot{Q}$ MRI utilizing arterial spin tagging in healthy volunteers as well as in patients after lung transplantation.

Whereas these approaches require the consecutive acquisition of ^{3}He and ^{1}H scans, Viallon et al. (134) demonstrated a complementary modality for the joint assessment of ventilation and perfusion in a single HP ^{3}He inhalation experiment. Relative blood volume maps of the lungs were generated based on the ^{3}He gas phase signal depletion during the first pass of a superparamagnetic contrast agent bolus. The simultaneous ventilation and perfusion assessments were demonstrated in normal rat lungs and were applied to an experimental animal model of pulmonary embolism. In patients with acute pulmonary embolism, it is expected that HP ^{3}He MRI will demonstrate homogeneous ventilation, while MR angiography or perfusion imaging will depict defects.

Spectroscopy and Imaging of Dissolved-Phase ^{129}Xe

Xenon dissolves in the lung parenchyma and blood, travels to distant organs, and accumulates in tissue, whereas He in general has poor solubility (Table 1). Besides the gas-phase resonance at 0 ppm, additional peaks around ~197 and ~212 ppm are thus evident in HP ^{129}Xe spectra of the chest (Fig. 9). These were attributed to the lung parenchyma and Xe inside red blood cells, respectively (14,15,18,135,136). The origin of a third peak at ~188 ppm has not yet been unambiguously identified but may be due

to epicardial fat (135). As it freely diffuses across biological membranes and is metabolically inert, radioactive ^{133}Xe has been used in nuclear medicine to study perfusion based on the principles of diffusible tracers as outlined by Kety (137). Similar experiments may be performed with HP ^{129}Xe MRI. Several authors presented theoretical models describing the exchange of ^{129}Xe between the alveolar space, blood, and tissues and considering the relaxation properties in such environments (138–140). Swanson et al. (135,141) used 1D and 2D chemical-shift selective spectroscopic imaging (CSI (142)) of the chest and the brain to study the distribution and time course of ^{129}Xe resonances. Analysis of the uptake and washout of HP ^{129}Xe in the gas and tissue phases demonstrates a potential for measuring regional blood flow, cardiac perfusion, kidney perfusion, and lung function.

A major challenge for the application of dissolved-phase HP ^{129}Xe for in vivo studies is its much weaker signal than that of the gas-phase resonance (143). With current respiration methods, the dissolved Xe is diluted throughout the body via blood flow from the lungs. Furthermore, as ^{129}Xe T_1 in blood is on the order of seconds (144–147), loss of hyperpolarization can occur before accumulation of a significant concentration is achieved even with prolonged ventilation. As an alternative, Ruppert et al. (65,136) performed magnetization-transfer experiments in dogs. After selectively saturating the resonance of ^{129}Xe dissolved in the lung parenchyma, partial depolarization was observed in the gas phase due to rapid Xe exchange between both compartments. This ^{129}Xe-polarization-transfer contrast (XTC) allows information about lung tissue to be obtained by imaging the gas-phase signal with its considerably higher intensity. Such investigations potentially provide information on the alveolar surface area or lung perfusion. The XTC technique has been successfully applied to the differentiation of extra- and intrapulmonary gas in a rabbit air-leak model (148).

Intravascular Delivery of Hyperpolarized Noble Gases

In nuclear medicine, injections of radioactive ^{133}Xe predissolved in saline to study regional blood flow were introduced in 1964 (149). As a similar approach for MRI, injection of HP noble gas inside a suitable carrier was suggested for improving the SNR of blood vessels or tissues relative to values attainable by respiration (143). The first in vivo images were obtained of the thigh muscle in a rat following the injection of an HP ^{129}Xe/saline solution into the upper hindleg (150). Other biologically compatible carriers, in which high concentrations of ^{129}Xe and long polarization lifetimes can be achieved, include lipid emulsions, perfluorocarbon compounds, or gas-filled liposomes (143,151–157). Using an HP ^{129}Xe/intralipid solution injected into a tail vein in rats, Möller et al. (152) obtained MR angiograms and local blood flow rates of the major pelvic and abdominal veins. More recently, the same carrier system was utilized by Duhamel et al. (155,156) for dynamic imaging of rat brain after injection into the carotid artery. To exploit the considerable signal advantage of ^{3}He (see above) while dealing with its poor solubility in fluids, Chawla et al. (158) investigated suspending HP ^{3}He within microbubbles. This approach per-

mitted angiographic images to be obtained following intravenous or intraarterial injections in rats. An advanced method is the encapsulation of HP ³He in biologically compatible microspheres, which reduces the risk of pulmonary embolism due to accumulation of bulk gas (159). With this technique, preliminary in vivo perfusion results have been produced in rats (160–163) and imaging the coronary arteries in an isolated pig heart was demonstrated (164).

MR MICROSCOPY IN SMALL ANIMALS

The first studies in HP gas imaging were performed in small animals for obvious safety reasons (10,11). An additional benefit was realized as HP gas supplies greatly exceeded small-animal lung volumes—liters compared to a few milliliters. Thus, multiple experiments can be done in a single day or high-resolution studies can be done in a single animal. Early small-animal measurements were also critical in addressing the complex interplay between motion of the polarized spins, choice of appropriate excitation parameters, and the dynamics of spin depolarization in vivo (14,64,78,79,96). Thus, animal studies provided the foundation of the physical interaction between polarized spins and their biological and physical environment to guide the development of relevant human protocols and more sophisticated methods for the basic scientists. An initial application of HP gas MRI in animals was gas density imaging to detect ventilation defects. In an image, signal voids depict airspaces where gas is unable to flow. Hedlund et al. (165) demonstrated this by using HP ³He MRI to find pulmonary airway obstruction in a controlled animal model.

Small animal models pose challenges in both space and time. Not only must one achieve higher spatial resolution than is common in clinical practice, one must also address the much more rapid physiologic time scales. As discussed above, the high diffusivity of gas will affect the resolution in an image; this leads to the fundamental problem of the resolution limit in HP gas MRI (166). Practical barriers that must be overcome for exploring the resolution limit experimentally include motion and limited SNR. Taking into account of the lung microstructure, which restricts the random motion of the gas, the resolution limit imposed by diffusion has been estimated to be 210 μm for ³He and 156 μm for ¹²⁹Xe (59). So for ³He, an isotropic voxel of $(210 \ \mu m)^3$ is $9.3 \times 10^{-3} \ mm^3$, ~1000 times smaller than the roughly 1 mm × 1 mm × 10 mm voxels typical in clinical studies. By utilizing and optimizing several technical aspects, a 3D image of the lungs in a live rat was obtained to experimentally explore these boundaries (12). A 468-μm slice from this dataset is shown in Fig. 10, with a pixel size of 117 × 117 μm. The problem of motion was addressed with the use of scan-synchronous ventilation with a fixed period (~700 ms) of held breath. During this relatively motionless period, a rapid RF pulse train (TR = 5 ms) was executed with radial PR. Additional use of variable flip angle excitation had the benefits of effectively extracting all the available magnetization stored in the given bolus of gas and minimizing view-to-view variations.

FIG. 10. Hyperpolarized ³He high-resolution coronal image of the lungs of a live adult rat. The pixel size is 117 × 117 μm and the slice thickness is 468 μm (12).

Figure 1 shows how much the resolution has increased in the brief period since the initial demonstration of HP gas MRI. It compares the very first ³He image acquired in a dead guinea pig (11) to an equivalent section of anatomy from a live rat acquired with the integrated methods outlined above. The Nyquist sampling in Fig. 1a is 280 μm × 560 μm × 10,000 μm (i.e., 1.57 mm³), while the sampling in Fig. 1b is 98 μm × 98 μm × 468 μm (i.e., 0.0045 mm³), an increase of more than 300-fold. The small airway labeled in Fig. 1b is at the 6th order of branching and is estimated to be ~100 μm in diameter.

Further modification of the radial PR sequence has allowed full and continuous sampling of the breathing cycle to obtain both a high spatial and temporal resolution. Figure 11 shows functional measurements in a guinea pig. The individual images in this composite image were encoded with pixels of 100 μm × 100 μm and temporal resolution of 50 ms (167). Panels a–c show the first 150 ms of an 800-ms period of inspiration, while panels d–f show the last 150 ms of the same interval. The technique of ventilatory synchronization (90) has been extended with a time division projection encoding sequence. Since the ventilatory pattern can be reliably reproduced, one can divide the pattern into small time increments, which are themselves reproducible. A limited number of views (between 5 and 20) are then acquired in each interval. The breathing cycle and pulse sequence are repeated a sufficient number of times (~50–200) to acquire a sufficient sample of k-space to support microscopic resolution at very short time intervals.

Technical developments required for accurate in vivo measurements of the physical parameters and extension of the spatial resolution to the microscopic regime have
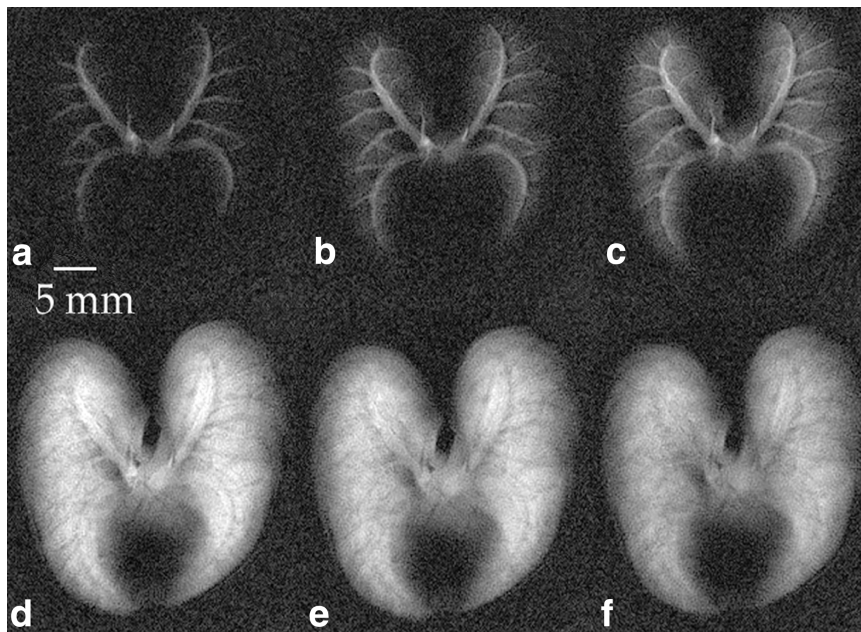
FIG. 11. Selected axial slices from a set of 16 HP ³He images measured in a guinea pig (slice thickness is 16 mm, field-of-view is 37 mm). With appropriate parsing of the views, "subimages" are obtained from the same dataset with temporal resolution of 50 ms. **a–c:** Images acquired in the early part of inspiration demonstrate substantial changes in airway filling; (**d,e**) breathhold images show uniform filling of the airspaces; (**f**) the first 50 ms of expiration show early emptying of the large airways as indicated by less signal intensity compared to **e**. Reproduced with permission from Viallon et al., Magn Reson Med 1999;41:787–792. © Wiley-Liss, Inc.

placed us in a position to explore physiologic and pathologic processes. It is not clear that the resolution limits in HP gas MRI have yet been reached, as the consequences of motion have not been adequately addressed. While scan-synchronous ventilation has minimized gross motion, it is not clear how reliably the technique returns the anatomy to the same position. While there is no signal from the heart, the motion of the heart must have some impact on the ³He signal as it pushes on adjacent lung tissue. Further technical work will be directed along these lines to find the experimental resolution limit.

CLINICAL IMAGING

Imaging human lung airspaces began soon after research in animals began. To deal with the insufficient quantities of gas—HP gas volumes are on the order of a single breath—researchers have diluted HP gas breaths with nitrogen. Hyperpolarized gas MRI has the potential to visualize lung airspaces at unpreceeded resolutions and provide mea-

sures of function. Present research is timely as current techniques for ventilation imaging like planar scintigraphy are generally regarded as insufficient to keep up with ongoing therapeutic developments—such as volume-reduction surgery, tumor resections, and thoracoscopic procedures.

Gas Density Imaging

A typical human ³He density study requires a breathhold period of ~10 sec to obtain ~10 coronal slices encompassing the entire lung. The signal is generally high (SNR > 10), and the spatial resolution (2.5 mm × 2.5 mm × 10 mm with gaps of 2–5 mm between slices) is significantly better than in nuclear medicine. Measurements of signal intensities can be used to depict regions which are preferentially ventilated. In normal human subjects, there is a trend towards preferential ventilation of the posterior lung areas in the supine position (168). Volume measurements have been made with good correlations from pulmonary

FIG. 12. Coronal HP ³He image of the posterior aspects of the lungs in a normal volunteer. **a:** Several small ventilation defects are seen in supine position. **b:** An image at the same anatomical level with the subject positioned prone shows almost homogeneous signal distribution.
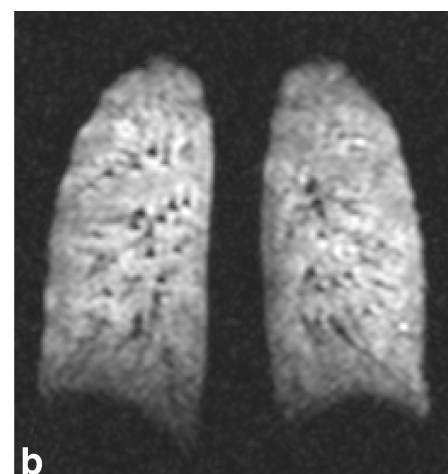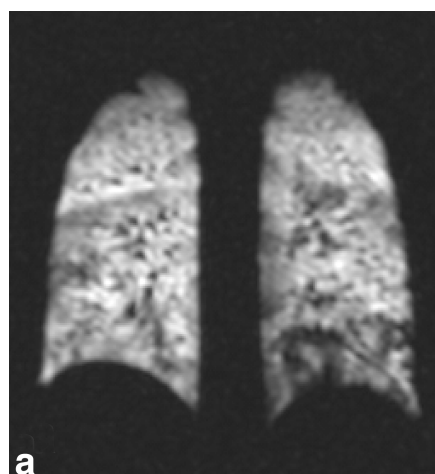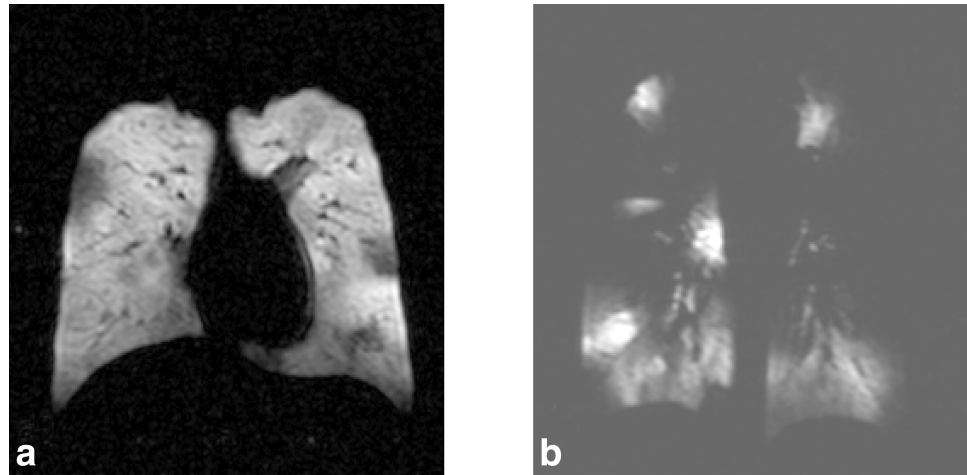
FIG. 13. Coronal HP ^{3}He lung images recorded in patients with cystic fibrosis. **a:** A patient with mild disease and normal spirometry (FEV$_1$ = 91% of predicted) shows few peripheral ventilation defects. **b:** A patient with severe cystic fibrosis (FEV$_1$ = 41% of predicted) has extensive ventilation defects.

function tests (169,170). In principle, estimations of absolute lung volumes are possible after appropriate corrections are made for airspace-to-tissue ratio, posture, and tidal volume. However, current standard deviations are high and the reproducibility is insufficient.

Complete and homogeneous distribution of the ^{3}He signal within the lung represents normal ventilation (171). In addition, transient ventilation defects that are less than 2 cm in size and located in the posterior lung fields are regarded as normal in healthy nonsmokers (172). These defects are likely the result of positional atelectasis. They appear when subjects are in the supine position (Fig. 12) and are regarded as physiological effects attributed to posture (173). In contrast to these small ventilation defects in normal volunteers, which illustrate the sensitivity of ^{3}He MRI, more widespread ventilation defects or inhomogeneities of signal distribution indicate impaired regional ventilation (171). The exact threshold between physiological variations and pathological findings has yet to be determined (68,129).

Smoking

Tobacco smoking causes damage to the airways. Initially, it affects small airways, leading to chronic inflammation and obstruction of the respiratory bronchioles. In a preliminary prospective study with five clinically healthy smokers and five nonsmokers, ventilation defects were only found in the smokers (168). Mean forced expiratory volume in 1 sec (FEV$_1$) was normal in all subjects. Ventilation defects per slice were counted. Smokers with normal pulmonary function tests had a median score of 1.1 (range 0.8–6.0) and nonsmokers had a score of 0.4 (range 0.1–0.8). This is a strong indication that ^{3}He MRI may allow detection of the effects of smoking in clinically healthy smokers. With FEV$_1$ being normal, ^{3}He MRI could be used to detect potentially reversible airway disease at an early stage.

Chronic Obstructive Pulmonary Disease and Emphysema

Chronic bronchitis is a widespread disease with enormous economic consequences. It is characterized by chronic inflammation of central and peripheral airways. When it results in obstruction due to mucosal thickening, airway narrowing, loss of elastic recoil, and expiratory collapse, it is referred to as chronic obstructive pulmonary disease (COPD). Frequently, COPD progresses and leads to destruction of alveolar walls with enlargement of peripheral airspaces (emphysema). De Lange et al. (68) investigated 13 healthy subjects and three subjects with a smoking history and COPD. Extensive ventilatory defects were found in a patient with known severe emphysema and corresponded to defects seen with ^{133}Xe ventilation scintigraphy several months earlier. Emphysema and COPD were associated with multiple round or wedge-shaped, patchy or widespread, small or large ventilation defects with whole segments or lobes involved (171,174). It is speculated that certain patterns of size and shape of ventilation defects indicate the site of obstruction, which may be located in the central or peripheral bronchi or even at the level of the bronchioles.

Cystic Fibrosis and Bronchiectasis

Cystic fibrosis and bronchiectasis are characterized by dilated central and peripheral bronchi. They are frequently associated with bronchial wall thickening. Subsequently, these changes lead to mucous plugging, chronic infection, as well as delayed and impaired ventilation of distal airspaces. Donnelly et al. (69) investigated four patients with cystic fibrosis. In all subjects, ventilation abnormalities were seen in all lung zones using ^{3}He MRI despite minimal or minor morphologic abnormalities on proton images. Ventilation defects were widespread and ranged from wedge-shaped peripheral defects to huge signal voids in entire lung zones. There was a predominance of defects in the upper posterior lung zones, whereas the lower lung zones were the least affected. The severity of the ^{3}He findings yielded a good correlation with abnormalities observed with pulmonary function tests. In another small series of patients with cystic fibrosis (Fig. 13), ventilation defects were seen in a subject with clinically mild disease and normal spirometry, suggesting that ^{3}He MRI may be a sensitive test for early changes of the disease (175). This
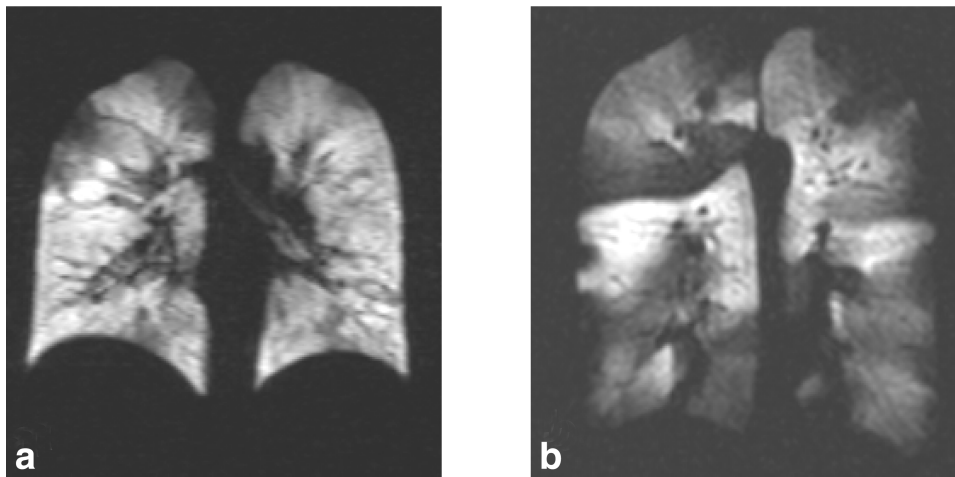
FIG. 14. Coronal HP ³He lung images recorded in patients with asthma. **a:** A patient with mild disease and normal spirometry ($FEV_1 = 98\%$ of predicted) shows a few pleural-based peripheral ventilation defects. **b:** A patient with severe asthma ($FEV_1 = 36\%$ of predicted) has a large number of defects.

finding is potentially important because early treatment may improve the long-term outcome. In another patient with extensive ventilation defects, ³He MRI showed improvement following chest physical therapy (image not shown).

Asthma

Asthma is a disease characterized by chronic inflammation and reversible obstruction of the small airways resulting in impaired pulmonary ventilation. Although clinical disease activity can be followed indirectly by pulmonary function testing and symptom reporting, asymptomatic asthmatics may have significant airway inflammation, which can only be detected using invasive tests such as bronchoscopy. It has been shown with ³He MRI that asthmatics have ventilation defects, even when asymptomatic from normal lung function testing (173). Preliminary results indicate that patients with severe asthma have larger and more ventilation defects than those with mild disease (Fig. 14). In addition, it was demonstrated that partial or complete reversal of the ventilation defects occurred after inhalation of a bronchodilator (Fig. 15). Hyperpolarized ³He MRI therefore appears to be a sensitive test for assessing ventilation changes in the lung of asthmatic patients.

Lung Transplantation and Bronchiolitis Obliterans

Lung transplantation is the ultimate treatment option in end-stage lung disease. Chronic rejection is the most important limitation of long-term survival of these patients. The immune reaction of chronic rejection mainly takes place in the small airways and is a form of bronchiolitis obliterans. Early diagnosis is extremely difficult because changes are subtle—only revealed by histologic examination. However, early diagnosis may improve treatment and prolong survival. All six lung-transplant patients of a preliminary study had ventilatory defects with ³He MRI (176). The extent of the defects correlated with the severity of bronchiolitis obliterans using an established clinical grading system. In comparison with scintigraphy and CT, ³He MRI proved to be more sensitive in the detection of ventilation defects. Different studies in single lung transplant recipients showed preferential ventilation of the nonrejected transplant in comparison with the native lung by a significantly higher signal intensity (177). In addition to bronchiolitis obliterans, small ventilation defects in the

FIG. 15. Coronal HP ³He imaging of the lungs from a patient with mild asthma ($FEV_1 = 100\%$ of predicted). **a:** At first, several small peripheral ventilation defects are detected. **b:** Thirty minutes after inhalation of a bronchodilator (Albuterol), the ³He image indicates that the defects have been filled, although there was no significant change in spirometry ($FEV_1 = 104\%$ of predicted).
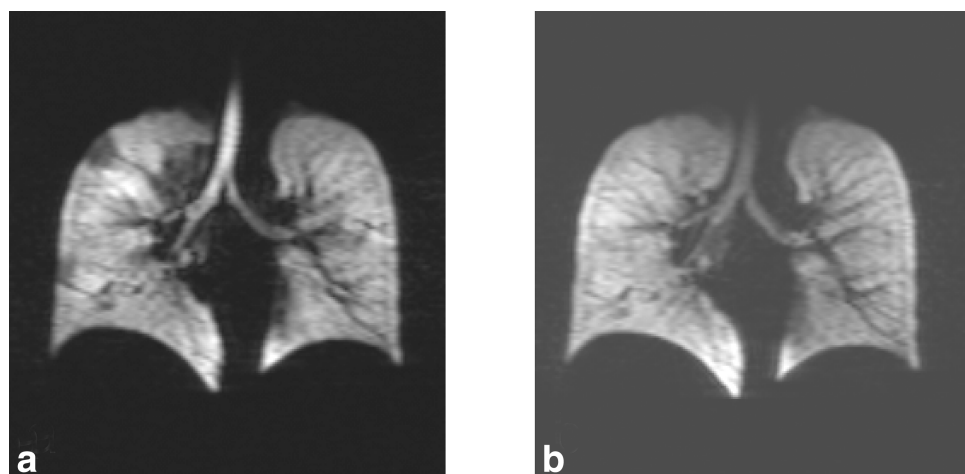
transplanted lung were caused by postoperative changes and pleural effusion. Large or numerous ventilation defects observed in the transplanted lung indicated bronchiolitis or pneumonia.

Beyond Static Ventilation Imaging

Because the correlation between the severity of ventilation defects and the clinical ventilatory function has not yet been evaluated, the sensitivity of HP gas MRI in assessing lung function is unknown. Initial experience from static ventilation studies showed a relatively low specificity in diagnosing lung diseases. Exploiting additional HP gas techniques may thus be helpful to improve specificity, characterize the disease processes, and obtain functional information.

Dynamic Imaging

The first demonstration of dynamic imaging was by Mac-Fall et al. (17) using GRE imaging on two 20-mm coronal slices (time resolution 1800 ms, matrix size 256 × 128). Inflow of gas was very rapid as signal in the apex and middle of the lung appeared almost immediately. This technique was modified using imaging times of 130 ms on coronal projections (178). Both the inspiratory and expiratory phases of respiration were observed, with images tracking the ^{3}He bolus traveling through the trachea, mainstem bronchi, subsequent bronchi, and alveolar spaces. Using a faster time resolution (122 ms) by employing single-shot EPI on three 10-mm axial slices, a steady influx of HP ^{3}He was observed, showing distal airspaces with signal within the first 200 ms (67). A dependent effect was observed with 50% higher signal intensities in posterior sections of the lung (subject was supine). The drawback of using the faster imaging sequences is the decrease in resolution—matrix sizes are typically no bigger than 64 × 64. However, this is sufficient for analysis of signal intensity dynamics in various parts of the lung.

Using dynamic imaging, functional lung ventilation can be directly assessed, yielding information about the ventilation distribution (179). While normal subjects demonstrate rapid filling of the lungs, it is expected that diseased lungs with changed lung compliance or airway blockage will lead to a changed pattern for ventilation. Echo-planar and interleaved-spiral sequences were used to achieve real-time visualization of inhalation and washout of HP ^{3}He in normal and diseased lungs (67,179,180). In healthy volunteers, the uniform segmental washin and washout of the gas in the lungs were demonstrated in great detail. The distribution of the lung filling was much more heterogeneous in patients with known lung disease (180). Patients with smoking-related centrilobular emphysema showed inhomogeneous sequential filling of their airspaces with interspersed ventilation defects (179). While rebreathing ^{3}He from a bag, the distribution gradually became more homogeneous. As expected, there was a predominance of abnormalities in the upper lobes in centrilobular emphysema. The results demonstrate that HP ^{3}He MRI is capable of visualizing different pulmonary compartments by distribution analysis. In comparison with CT, areas with the

a

b

c
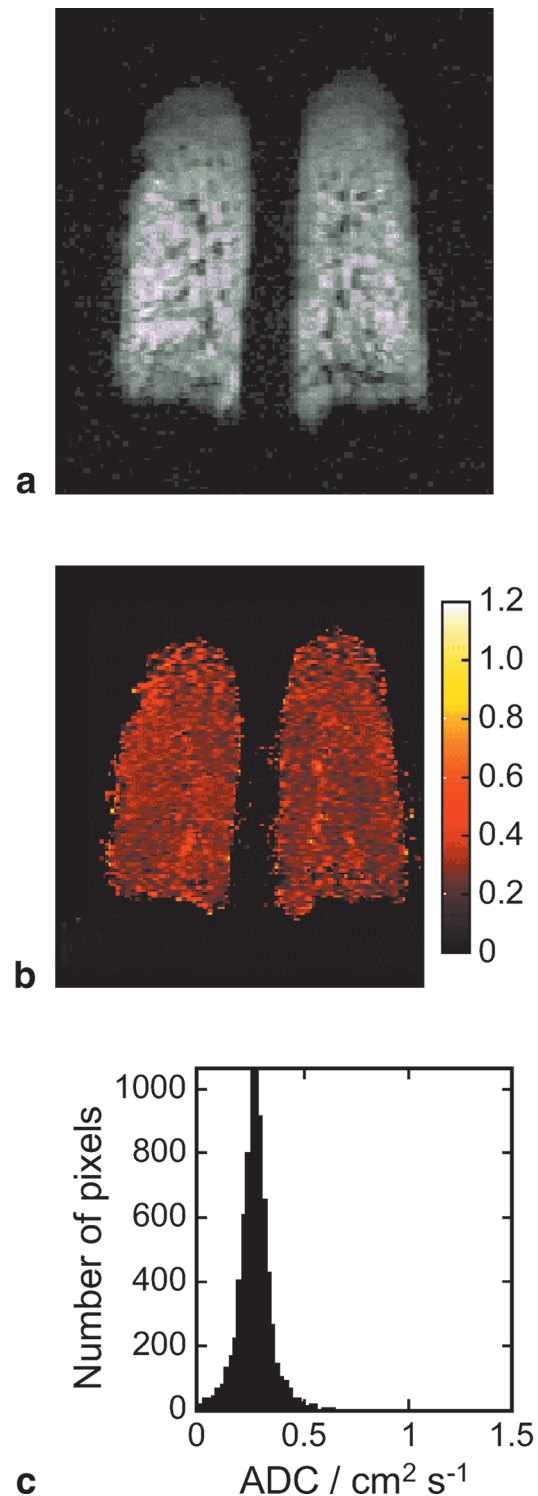
FIG. 16. Diffusion imaging of a healthy, nonsmoking volunteer in the coronal plane. **a:** The zero-weighted diffusion image demonstrates homogeneous distribution of the HP ^{3}He gas signal. **b:** The corresponding ADC map and (**c**) histogram show a homogeneous distribution of ADC values with little variation (mean: 0.28 ± 0.11 cm^2/s).

most severe emphysematous destruction showed delayed or lacking ventilation at ^{3}He MRI. During expiration, washout from emphysematous regions was prolonged, indicating airtrapping.

Diffusion Imaging in Patients

Diffusion studies in healthy volunteers showed small, homogeneously distributed ADCs with typical mean values between 0.17 and 0.28 cm^2/s (Fig. 16). By contrast, in severely emphysematous patients ADC values were inhomogeneously distributed and values increased up to a factor of 2.5 (between 0.40 and 0.90 cm^2/s), indicating enlargement of airspaces (120,121,181) (Fig. 17). Typically, diffusivity histograms in patients were substantially broader than those in healthy volunteers (122). The regional variation was consistent with a centrilobular distribution and the values correlated with pulmonary function tests (182). Hanisch et al. (183) measured the ADC in the trachea (0.67 cm^2/s), in the normal lung parenchyma (0.13 cm^2/s) and in fibrosis with honeycombing (0.35 cm^2/s). While gas diffusion was almost isotropic in the alveolar space and the peripheral airways in normal subjects, it was anisotropic in the diseased lung. This finding indicates that nonspherical geometrical changes may be responsible for a preferential direction for diffusive gas motion.

CONCLUSIONS AND FUTURE PROSPECTS

Hyperpolarized gas MRI was first introduced in 1994 and the enormous advances made in the last years will almost certainly lead the way to routine clinical application as well as new paths in animal research. Without the need for using harmful ionizing radiation, HP gas MRI extends the principle of functional imaging to the lung and can be applied for repeated studies during follow-up as well as in the pediatric population. Small-animal imaging has been critical in defining the methods required for human studies and providing the necessary stable platform for the quantitative measurements of the in vivo physical parameters of HP gas. As the pharmaceutical community realizes the quantitative metrics that HP gas MRI can provide, it has become clear that cost-effective quantitative measures of structure and function may be obtained. Potential pulmonary drugs, previously validated with histology and spirometry, can now be evaluated in longitudinal studies with regional specificity, and there is a clear path from mouse to man.

Novel strategies for MRI of the lungs, which are currently being pursued, are not limited to the application of HP noble gases. Edelman et al. (184) used ^{1}H MRI combined with inhalation of 100% O_2 as a paramagnetic contrast agent to assess ventilation indirectly. Aerosolized gadopentetate dimeglumine has also been utilized to increase the proton signal in ventilation imaging (128). Another method for direct ventilation imaging is the use of inert fluorinated gases (e.g., CF_4, C_2F_6, or SF_6) and ^{19}F MRI (185–188). Such techniques, which are easy to implement and inexpensive, might prove to be useful in pulmonary imaging (187). However, HP gases offer superior SNR, spatial resolution, speed of imaging, and an immense range of experimental approaches to yield detailed information on morphology and function.

To date, the clinical focus of HP gas has been on ventilation studies with [3]He, but there are many other possibilities. Utilizing diffusion has already demonstrated appli-

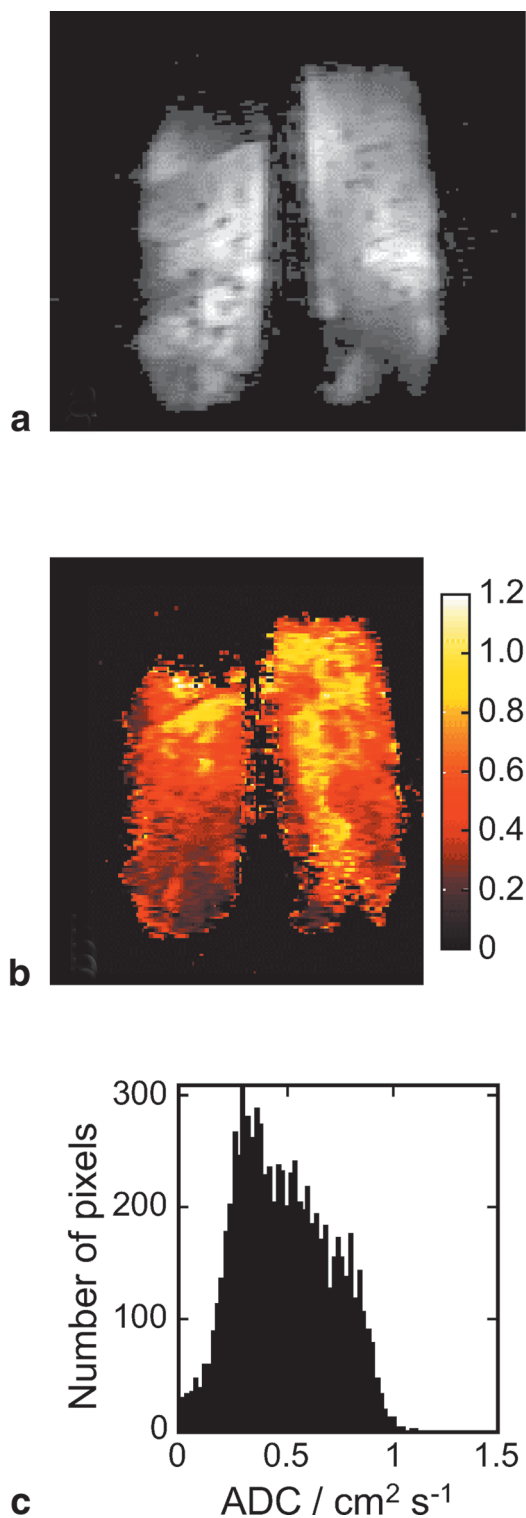FIG. 17. Diffusion imaging of a patient with COPD in the coronal plane. **a:** The zero-weighted diffusion image shows heterogeneous distributions of the HP [3]He gas signal, particularly in the upper lobes. **b:** The corresponding ADC map reflects the same trend with a varying range of ADC values. **c:** Measurements from the histogram show an increase in ADC values and substantial variation (mean: 0.51 ± 0.22 cm^2/s).

cability in diagnosing emphysema. Regions exhibiting a $\dot{V}/\dot{Q}$ mismatch may be identified by changes in p_{O2} and, hence, abnormal T_1. T_2^*-weighted MRI may provide information about changes in the tissue composition related to disease if sufficient BMS variations are produced. The solubility and lipophilic properties of Xe holds promise for functional MRI. Its binding to hemoglobin has been utilized to measure blood oxygenation (189). Specific molecular target recognition via the chemical-shift sensitivity of ^{129}Xe may be achieved with biosensor molecules designed to bind both Xe and protein (190). Injection of suitable carrier agents for HP noble gases introduces a novel class of contrast agents. Advantages include intravascular confinement, lack of background signal, and limited recirculation, suggesting a potential for perfusion measurements. Another unique aspect, which has not yet been utilized for in vivo applications, is the enhancement of signals of other nuclei (e.g., ^{1}H (191) or ^{13}C (192)) in contact with the HP gas atoms via cross-relaxation. Using a single-resonance method dubbed SPINOE (spin polarization-induced nuclear Overhauser effect), which combines OP and the nuclear Overhauser effect, Navon et al. (193) have shown that it is possible not only to image HP gas directly but also the environment in which it is accommodated. This opens a window for studying proteins or membranes (194).

There is little doubt that HP noble gases will have a revolutionary impact on MRI of the lungs. For further evaluation of ventilation imaging, which is being applied in clinical practice, quantitative comparisons with established modalities such as scintigraphic techniques and pulmonary function tests on a larger population are warranted. Methodologies utilizing other parameters than spin density are more challenging because less intense signal is produced. However, the potential benefit for both basic and clinical scientists is extraordinary.

ACKNOWLEDGMENTS

REFERENCES

1. Lauterbur PC. Image formation by induced local interactions: examples employing nuclear magnetic resonance. Nature 1973;242:190–191.
2. Kastler A. Quelques suggestions concernant la production optique et la détection optique d'une inégalité de population des niveaux de quantification spatiale des atomes. Application à l'expérience de Stern et Gerlach et à la résonance magnétique. J Phys Radium 1950;11:255–265.
3. Raftery D, Long H, Meersmann T, Grandinetti PJ, Reven L, Pines A. High-field NMR of adsorbed xenon polarized by laser pumping. Phys Rev Lett 1991;66:584–587.
4. Zeng X, Wu C, Zhao M, Li S, Li L, Zhang X, Liu Z, Liu W. Laser-enhanced low-pressure gas NMR signal from ^{129}Xe. Chem Phys Lett 1991;182:538–540.
5. Tycko R, Reimer JA. Optical pumping in solid state nuclear magnetic resonance. J Phys Chem 1996;100:13240–13250.
6. Goodson BM, Kaiser L, Pines A. NMR and MRI of laser-polarized noble gases in molecules, materials, and medicine. In: Maraviglia B, editor. Magnetic resonance and brain function: approaches from physics. Amsterdam: IOS Press; 1999. p 211–260.
7. Brunner E. Enhancement of surface and biological magnetic resonance using laser-polarized noble gases. Concepts Magn Reson 1999;11:313–335.
8. Pietraβ T. Optically polarized ^{129}Xe in magnetic resonance techniques. Magn Reson Rev 2000;17:263–337.
9. Cutillo AG, editor. Application of magnetic resonance to the study of lung. Armonk: Futura Publishing; 1996.
10. Albert MS, Cates GD, Driehuys B, Happer W, Saam B, Springer CS, Wishnia A. Biological magnetic resonance imaging using laser-polarized ^{129}Xe. Nature 1994;370:199–201.
11. Middleton H, Black RD, Saam B, Cates GD, Cofer GP, Guenther R, Happer W, Hedlund LW, Johnson GA, Juvan K, Swarz J. MR imaging with hyperpolarized ^{3}He gas. Magn Reson Med 1995;33:271–275.
12. Johnson GA, Cofer GP, Hedlund LW, Maronpot RR, Suddarth SA. Registered ^{1}H and ^{3}He magnetic resonance microscopy of the lung. Magn Reson Med 2001;45:365–370.
13. Black RD, Middleton HD, Cates GD, Cofer GP, Driehuys B, Happer W, Hedlund LW, Johnson GA, Shattuck MD, Swartz JC. In vivo He-3 MR images of guinea pig lungs. Radiology 1996;199:867–870.
14. Wagshul ME, Button TM, Li HF, Liang Z, Springer CS, Zhong K, Wishnia A. In vivo MR imaging and spectroscopy using hyperpolarized ^{129}Xe. Magn Reson Med 1996;36:183–191.
15. Sakai K, Bilek AM, Oteiza E, Walsworth RL, Balamore D, Jolesz FA, Albert MS. Temporal dynamics of hyperpolarized ^{129}Xe resonances in living rats. J Magn Reson B 1996;111:300–304.
16. Ebert M, Grossmann T, Heil W, Otten WE, Surkau R, Leduc M, Bachert P, Knopp MV, Schad LR, Thelen M. Nuclear magnetic resonance imaging with hyperpolarised helium-3. Lancet 1996;347:1297–1299.
17. MacFall JR, Charles HC, Black RD, Middleton H, Swartz JC, Saam B, Driehuys B, Erickson C, Happer W, Cates GD, Johnson GA, Ravin CE. Human lung air spaces: potential for MR imaging with hyperpolarized He-3. Radiology 1996;200:553–558.
18. Mugler JP, Driehuys B, Brookeman JR, Cates GD, Berr SS, Bryant RG, Daniel TM, de Lange EE, Downs JH, Erickson CJ, Happer W, Hinton DP, Kassel NF, Maier T, Phillips CD, Saam BT, Sauer KL, Wagshul ME. MR imaging and spectroscopy using hyperpolarized ^{129}Xe gas: preliminary human results. Magn Reson Med 1997;37:809–815.
19. Kauczor HU, Hofmann D, Kreitner KF, Nilgens H, Surkau R, Heil W, Potthast A, Knopp MV, Otten EW, Thelen M. Normal and abnormal pulmonary ventilation: visualization at hyperpolarized He-3 MR imaging. Radiology 1996;201:564–568.
20. Leawoods JC, Yablonskiy DA, Saam B, Gierada DS, Conradi MS. Hyperpolarized ^{3}He gas production and MR imaging of the lung. Concepts Magn Reson 2001;13:277–293.
21. Kauczor HU, Chen XJ, van Beek EJR, Schreiber WG. Pulmonary ventilation imaged by magnetic resonance: at the doorstep of clinical application. Eur Respir J 2001;17:1–16.
22. Frossati G. Polarization of ^{3}He, D$_2$ and (eventually) ^{129}Xe using low temperatures and high magnetic fields. J Low Temp Phys 1998;111:521–532.
23. Akimoto H, van Rooijen R, Jochemsen R, Frossati G, van Saarloos W. Melting process and interface instability of highly magnetized solid ^{3}He: role of the magnetization gradient. Phys Rev Lett 2000;85:1894–1897.
24. Walker TG, Happer W. Spin-exchange optical pumping of noble-gas nuclei. Rev Mod Phys 1997;69:629–642.
25. Happer W, van Wijngaarden WA. An optical pumping primer. Hyperfine Interact 1987;38:435–470.
26. Happer W. Optical pumping. Rev Mod Phys 1972;44:169–249.
27. Appelt S, Ben-Amar Baranga A, Erickson CJ, Romalis MV, Young AR, Happer W. Theory of spin-exchange optical pumping of ^{3}He and ^{129}Xe. Phys Rev A 1998;58:1412–1439.
28. Ben-Amar Baranga A, Appelt S, Romalis MV, Erickson CJ, Young AR, Cates GD, Happer W. Polarization of ^{3}He by spin exchange with optically pumped Rb and K vapors. Phys Rev Lett 1998;80:2801–2804.
29. Schearer LD, Walters GK. Nuclear spin-lattice relaxation in the presence of magnetic-field gradients. Phys Rev 1965;139:A1398–A1402.
30. Cates GD, Schaefer SR, Happer W. Relaxation of spins due to field inhomogeneities in gaseous samples at low magnetic fields and low pressures. Phys Rev A 1988;37:2877–2885.
31. Chupp TE, Hoare RJ, Walsworth RL, Wu B. Spin-exchange-pumped ^{3}He and ^{129}Xe Zeeman masers. Phys Rev Lett 1994;72:2363–2366.

32. Colegrove FD, Schearer LD, Walters GK. Polarization of ^{3}He gas by optical pumping. Phys Rev 1963;132:2561–2572.

33. Gentile TR, McKeown RD. Spin-polarizing ^{3}He nuclei with an arc-lamp-pumped neodymium-doped lanthanum magnesium hexaluminate laser. Phys Rev A 1993;47:456–467.

34. Stoltz E, Meyerhoff M, Bigelow N, Leduc M, Nacher PJ, Tastevin G. High nuclear polarization in ^{3}He and ^{3}He-^{4}He gas mixtures by optical pumping with a laser diode. Appl Phys B 1996;63:629–633.

35. Becker J, Heil W, Krug B, Leduc M, Meyerhoff M, Nacher PJ, Otten EW, Prokscha T, Schearer LD, Surkau R. Study of mechanical compression of spin-polarized ^{3}He gas. Nucl Instrum Meth A 1994;346: 45–51.

36. Becker J, Bermuth J, Ebert M, Grossmann T, Heil W, Hofmann D, Humblot H, Leduc M, Otten EW, Rode D, Surkau R. Interdisciplinary experiments with polarized ^{3}He. Nucl Instrum Meth A 1998;402:327–336.

37. Nacher PJ, Tastevin G, Maître X, Dollat X, Lemaire B, Olejnik J. A peristaltic compressor for hyperpolarised helium. Eur Radiol 1999;9: B18.

38. Gentile TR, Jones GL, Thompson AK, Rizi RR, Roberts DA, Dimitrov IE, Reddy R, Lipson DA, Gefter W, Schnall MD, Leigh JS. Demonstration of a compact compressor for application of metastability-exchange optical pumping of ^{3}He to human lung imaging. Magn Reson Med 2000;43:290–294.

39. Harris RK. Nuclear spin properties and notation. In: Grant DM, Harris RK, editors. Encyclopedia of nuclear magnetic resonance. Chichester, UK: Wiley; 1996. p 3301–3314.

40. Seydoux R, Diehl P, Mazitov RK, Jokisaari J. Chemical shifts in magnetic resonance of the ^{3}He nucleus in liquid solvents and comparison with other noble gases. J Magn Reson A 1993;101:78–83.

41. Miller KW, Reo NV, Schoot Uiterkamp AJM, Stengle DP, Stengle TR, Williamson KL. Xenon NMR: chemical shifts of a general anesthetic in common solvents, proteins, and membranes. Proc Natl Acad Sci USA 1981;78:4946–4949.

42. Newbury NR, Barton AS, Cates GD, Happer W, Middleton H. Gaseous ^{3}He-^{3}He magnetic dipolar relaxation. Phys Rev A 1993;48:4411–4420.

43. Hunt ER, Carr HY. Nuclear magnetic resonance of Xe^{129} in natural xenon. Phys Rev 1963;130:2302–2305.

44. Saam B, Happer W, Middleton H. Nuclear relaxation of ^{3}He in the presence of O_2. Phys Rev A 1995;52:862–865.

45. Jameson CJ, Jameson AK, Hwang JK. Nuclear spin relaxation by intermolecular magnetic dipole coupling in the gas phase. ^{129}Xe in oxygen. J Chem Phys 1988;89:4074–4081.

46. Chen XJ, Möller HE, Chawla MS, Cofer GP, Driehuys B, Hedlund LW, MacFall JR, Johnson GA. Spatially resolved measurements of hyperpolarized gas properties in the lung in vivo. I. Diffusion coefficient. Magn Reson Med 1999;42:721–728.

47. Weathersby PK, Homer LD. Solubility of inert gases in biological fluids and tissues: a review. Undersea Biomed Res 1980;7:277–296.

48. Fitzsimmons WA, Tankersley LL, Walters GK. Nature of surface-induced nuclear spin relaxation. Phys Rev 1969;179:156–165.

49. Jones GL, Gentile TR, Thompson AK, Chowdhuri Z, Dewey MS, Snow WM, Wietfeldt FE. Test of ^{3}He-based neutron polarizers at NIST. Nucl Instrum Meth A 2000;440:772–776.

50. Hsu MF, Cates GD, Kominis I, Aksay IA, Dabbs DM. Sol-gel coated glass cells for spin-exchange polarized ^{3}He. Appl Phys Lett 2000;77: 2069–2071.

51. Heil W, Dreyer J, Hofmann D, Humblot H, Lelievre-Berna E, Tasset F. ^{3}He neutron spin filter. Physica B 1999;267–268, 328–335.

52. Heil W, Humblot H, Otten E, Schafer M, Sarkau R, Leduc M. Very long nuclear relaxation times of spin polarized helium 3 in metal coated cells. Phys Lett A 1995;201:337–343.

53. Cates GD, Fitzgerald RJ, Barton AS, Bogorad P, Gatzke M, Newbury NR, Saam B. Rb-^{129}Xe spin-exchange rates due to binary and three-body collisions at high Xe pressure. Phys Rev A 1992;45:4631–4639.

54. Breeze SR, Lang S, Moudrakovski I, Ratcliffe CI, Ripmeester JA, Santyr S, Simard B Zuger I. Coatings for optical pumping cells and short-term storage of hyperpolarized xenon. J Appl Phys 2000;87:8013–8017.

55. Walker TG. Estimates of spin-exchange parameters for alkali-metal-noble-gas pairs. Phys Rev A 1989;40:4959–4964.

56. Rosen MS, Chupp TE, Coulter KP, Welsh RC, Swanson SD. Polarized ^{129}Xe optical pumping/spin exchange and delivery system for magnetic resonance spectroscopy and imaging studies. Rev Sci Instrum 1999;70:1546–1552.

57. Driehuys B, Cates GD, Miron E, Sauer K, Walter DK, Happer W. High-volume production of laser-polarized ^{129}Xe. Appl Phys Lett 1996;69:1668–1670.

58. Gatzke M, Cates GD, Driehuys B, Fox D, Happer W, Saam B. Extraordinarily slow nuclear spin relaxation in frozen laser-polarized ^{129}Xe. Phys Rev Lett 1993;70:690–693.

59. Möller HE, Chen XJ, Chawla MS, Cofer GP, Driehuys B, Hedlund LW, Suddarth SA, Johnson GA. Sensitivity and resolution in 3D NMR microscopy of the lung with hyperpolarized noble gases. Magn Reson Med 1999;41:800–808.

60. Luttropp HH, Thomasson R, Dahm S, Persson J, Werner O. Clinical experience with minimal flow xenon anesthesia. Acta Anaesthesiol Scand 1994;38:121–125.

61. Hoult DI, Lauterbur PC. The sensitivity of the zeugmatographic experiment involving human samples. J Magn Reson 1979;34:425–433.

62. Tseng CH, Wong GP, Pomeroy VR, Mair RW, Hinton DP, Hoffmann D, Stoner RE, Hersman FW, Cory DG, Walsworth RL. Low-field MRI of laser polarized noble gas. Phys Rev Lett 1998;81:3785–3788.

63. Wong GP, Tseng CH, Pomeroy VR, Mair RW, Hinton DP, Hoffmann D, Stoner RE, Hersman FW, Cory DG, Walsworth RL. A system for low field imaging of laser-polarized noble gas. J Magn Reson 1999;141: 217–227.

64. Johnson GA, Cates G, Chen XJ, Cofer GP, Driehuys B, Happer W, Hedlund LW, Saam B, Shattuck MD, Swartz J. Dynamics of magnetization in hyperpolarized gas MRI of the lung. Magn Reson Med 1997; 38:66–71.

65. Ruppert K, Brookeman JR, Hagspiel KD, Mugler JP. Probing lung physiology with xenon polarization transfer contrast (XTC). Magn Reson Med 2000;44:349–357.

66. Darasse L, Guillot G, Nacher PJ, Tastevin G. Low-field ^{3}He nuclear magnetic resonance in human lungs. CR Acad Sci II B 1997;324:691–700.

67. Saam B, Yablonskiy DA, Gierada DS, Conradi MS. Rapid imaging of hyperpolarized gas using EPI. Magn Reson Med 1999;42:507–514.

68. de Lange EE, Mugler JP, Brookeman JR, Knight-Scott J, Truwit JD, Teates CD, Daniel TM, Bogorad PL, Cates GD. Lung air spaces: MR imaging evaluation with hyperpolarized ^{3}He gas. Radiology 1999;210: 851–857.

69. Donnelly LF, MacFall JR, McAdams HP, Majure JM, Smith J, Frush DP, Bogorad P, Charles HC, Ravin CE. Cystic fibrosis: combined hyperpolarized ^{3}He-enhanced and conventional proton MR imaging in the lung—preliminary observation. Radiology 1999;212:885–889.

70. Deninger AJ, Eberle B, Ebert M, Großmann T, Heil W, Kauczor HU, Lauer L, Markstaller K, Otten E, Schmiedeskamp J, Schreiber W, Surkau R, Thelen M, Weiler N. Quantification of regional intrapulmonary oxygen partial pressure evolution during apnea by ^{3}He MRI. J Magn Reson 1999;141:207–216.

71. Mansfield P. Multi-planar image formation using NMR spin echoes. J Phys C 1977;10:L55–L58.

72. Ahn CB, Kim JH, Cho ZH. High-speed spiral-scan echo planar NMR imaging. IEEE Trans Med Imag 1986;MI-5;2–7.

73. Haase A, Frahm J, Matthaei D, Hänicke W, Merboldt KD. FLASH imaging. Rapid NMR imaging using low flip-angle pulses. J Magn Reson 1986;67:258–266.

74. Mugler JP. Optimization of gradient-echo sequences for hyperpolarized noble-gas MRI. In: Proc 6th ISMRM Scientific Meeting, Sydney, 1998. p 1904.

75. Bergin CJ, Pauly JM, Macovski A. Lung parenchyma: projection encoding MR imaging. Radiology 1991;179:777–781.

76. Gewalt SL, Glover GH, Hedlund LW, Cofer GP, MacFall JR, Johnson GA. MR microscopy of the rat lung using projection reconstruction. Magn Reson Med 1993;29:99–106.

77. Bachert P, Schad LR, Bock M, Knopp MV, Ebert M, Grossmann T, Heil W, Hofmann D, Surkau R, Otten EW. Nuclear magnetic resonance imaging of airways in humans with use of hyperpolarized He-3. Magn Reson Med 1996;36:192–196.

78. Möller HE, Chen XJ, Chawla MS, Driehuys B, Hedlund LW, Johnson GA. Signal dynamics in magnetic resonance imaging of the lung with hyperpolarized noble gases. J Magn Reson 1998;135:133–143.

79. Chen XJ, Chawla MS, Hedlund LW, Möller HE, MacFall JR, Johnson GA. MR microscopy of lung airways with hyperpolarized ^{3}He. Magn Reson Med 1998;39:79–84.

80. Stehling MK. Improved signal in "snapshot" FLASH by variable flip angles. Magn Reson Imag 1992;10:165–167.

81. Mugler JP, Epstein FH, Brookeman JR. Shaping the signal response during the approach to steady-state in three-dimensional magnetization-prepared rapid gradient-echo imaging using variable flip angles. Magn Reson Med 1992;28:165–185.

82. Sobering GS, Shiferaw Y. Optimization of acquisition parameters for multi-shot hyper-polarized NMR: variable flip angle excitation. In: Proc 3rd SMR Scientific Meeting, Nice, 1995. p 687.

83. Zhao L, Mulkern R, Tseng CH, Williamson D, Patz S, Kraft R, Walsworth RL, Jolesz FA, Albert MS. Gradient-echo imaging considerations for hyperpolarized ^{129}Xe MR. J Magn Reson B 1996;113:179–183.

84. Hennig J, Nauerth A, Friedburg H. RARE imaging: a fast imaging method for clinical MR. Magn Reson Med 1986;3:823–833.

85. Ruppert K, Brookeman JR, Mugler JP. Real-time MR imaging of pulmonary gas-flow dynamics with hyperpolarized ^{3}He. In: Proc 6th ISMRM Scientific Meeting, Sydney, 1998. p 1909.

86. Guillot G, Durand E, Vattolo D, Darasse L, Nacher PJ, Tastevin G. Human lung MRI of dilute ^{3}He: influence of gas composition. Eur Radiol 1999;9:B25.

87. Viallon M, Berthezène Y, Callot V, Bourgeois M, Humblot H, Briguet A, Crémillieux Y. Dynamic imaging of hyperpolarized ^{3}He distribution in rat lungs using interleaved-spiral scans. NMR Biomed 2000; 13:207–213.

88. Mugler JP, Brookeman JR, Knight-Scott J, Maier T, de Lange EE, Bogorad PL. Interleaved echo-planar imaging of the lungs with hyperpolarized ^{3}He. In: Proc 6th ISMRM Scientific Meeting, Sydney, 1998. p 448.

89. Ruppert K, Mugler JP. 3D hyperpolarized ^{3}He MR imaging of the lung using an interleaved-cylindrical k-space trajectory. In: Proc 9th ISMRM Scientific Meeting, Glasgow, 2001. p 945.

90. Hedlund LW, Cofer GP, Owen SJ, Johnson GA. MR-compatible ventilator for small animals: computer-controlled ventilation for proton and noble gas imaging. Magn Reson Imag 2000;18:753–759.

91. Ramirez MP, Sigaloff KCE, Kubatina LV, Donahue MA, Venkatesh AK, Albert MS. Physiological response of rats to delivery of helium and xenon: implications for hyperpolarized noble gas imaging. NMR Biomed 2000;13:253–264.

92. Hedlund LW, Möller HE, Chen XJ, Chawla MS, Cofer GP, Johnson GA. Mixing oxygen with hyperpolarized ^{3}He for small-animal lung studies. NMR Biomed 2000;13:202–206.

93. Eberle B, Weiler N, Markstaller K, Kauczor HU, Deninger A, Ebert M, Grossmann T, Heil W, Lauer LO, Roberts TPL, Schreiber WG, Surkau R, Dick WF, Otten EW, Thelen M. Analysis of intrapulmonary O_2 concentration by MR imaging of inhaled hyperpolarized helium-3. J Appl Physiol 1999;87:2043–2052.

94. Vold RL, Waugh JS, Klein MP, Phelps DE. Measurement of spin relaxation in complex systems. J Chem Phys 1968;48:3831–3832.

95. Look DC, Locker DR. Time saving in measurement of NMR and EPR relaxation times. Rev Sci Instrum 1970;41:50–51.

96. Möller HE, Hedlund LW, Chen XJ, Carey MR, Chawla MS, Wheeler CT, Johnson GA. Measurements of hyperpolarized gas properties in the lung. III. ^{3}He T_1. Magn Reson Med 2001;45:421–430.

97. Deninger AJ, Eberle B, Ebert M, Grossmann T, Hanisch G, Heil W, Kauczor HU, Markstaller K, Otten E, Schreiber W, Surkau R, Weiler N. ^{3}He-MRI-based measurements of intrapulmonary p_{O2} and its time course during apnea in healthy volunteers: first results, reproducibility, and technical limitations. NMR Biomed 2000;13:194–201.

98. Roberts D, Rizi R, Lipson DA, Hansen-Flaschen J, Yamomoto A, Gefter WB, Leigh JS, Schnall MS. Functional nonspecificity of T_1-weighted MRI of laser-polarized helium-3 gas. In: Proc 9th ISMRM Scientific Meeting, Glasgow, 2001. p 946.

99. Yablonskiy DA, Haacke EM. Theory of NMR signal behavior in magnetically inhomogeneous tissues—the static dephasing regime. Magn Reson Med 1994;32:749–763.

100. Durney CH, Bertolina J, Ailion DC, Christman R, Cutillo AG, Morris AH, Hashemi S. Calculation and interpretation of inhomogeneous line broadening in models of lungs and other heterogeneous structures. J Magn Reson 1989;85:554–570.

101. Ailion DC. Lung and mediastinum: a discussion of the relevant NMR physics. In: Grant DM, Harris RK, editors. Encyclopedia of nuclear magnetic resonance. Chichester, UK: Wiley; 1996. p 2867–2873.

102. Chen XJ, Chawla MS, Cofer GP, Hedlund LW, Möller HE, Johnson GA. Hyperpolarized ^{3}He NMR lineshape measurements in the live guinea pig lung. Magn Reson Med 1998;40:61–65.

103. Chen XJ, Möller HE, Chawla MS, Cofer GP, Driehuys B, Hedlund LW, MacFall JR, Johnson GA. Spatially resolved measurements of hyperpolarized gas properties in the lung in vivo. II. T_2^*. Magn Reson Med 1999;42:729–737.

104. Carr HY, Purcell EM. Effects of diffusion on free precession in nuclear magnetic resonance experiments. Phys Rev 1954;94:630–638.

105. Meiboom S, Gill D. Modified spin-echo method for measuring nuclear relaxation times. Rev Sci Instrum 1958;29:688–691.

106. de Swiet TM, Sen PN. Decay of nuclear magnetization by bounded diffusion in a contrast field gradient. J Chem Phys 1994;100:5597–5604.

107. Hürlimann MD. Effective gradients in porous media due to susceptibility differences. J Magn Reson 1998;131:232–240.

108. Case TA, Durney CH, Ailion DC, Cutillo AG, Morris AH. A mathematical model of diamagnetic line broadening in lung tissue and similar heterogeneous systems: calculations and measurements. J Magn Reson 1987;73:304–314.

109. Callaghan PT, Eccles CD. Diffusion-limited resolution in nuclear magnetic resonance microscopy. J Magn Reson 1988;78:1–8.

110. Stejskal EO, Tanner JE. Spin diffusion measurements: spin echoes in the presence of a time-dependent field gradient. J Chem Phys 1965; 42:288–292.

111. Patyal BR, Gao JH, Williams RF, Roby J, Saam B, Rockwell BA, Thomas RJ, Stolarski DJ, Fox PT. Longitudinal relaxation and diffusion measurements using magnetic resonance signals from laser-hyperpolarized ^{129}Xe nuclei. J Magn Reson 1997;126:58–65.

112. Bock M. Simultaneous T_2^* and diffusion measurements with ^{3}He. Magn Reson Med 1997;38:890–895.

113. Schmidt DM, George JS, Penttila SI, Caprihan A, Fukuschima E. Diffusion imaging with hyperpolarized ^{3}He gas. J Magn Reson 1997; 129:184–187.

114. Hirschfelder JO, Curtiss CF, Bird RB. Molecular theory of gases and liquids. New York: John Wiley & Sons; 1954.

115. Kliment V. Similarity and dimensional analysis, evaluation of aerosol deposition in the lungs of laboratory animals and man. Folia Morph (Warsz) 1973;21:59–64.

116. Stoller SD, Happer W, Dyson FJ. Transverse spin relaxation in inhomogeneous magnetic fields. Phys Rev A 1991;44:7459–7477.

117. Saam B, Drukker N, Happer W. Edge enhancement observed with hyperpolarized ^{3}He. Chem Phys Lett 1996;263:481–487.

118. Song YQ, Goodson BM, Sheridan B, de Swiet TM, Pines A. Effects of diffusion on xenon gas MRI. J Chem Phys 1998;108:6233–6239.

119. Mugler JP, Brookeman JR, Knight-Scott J, Maier T, de Lange EE, Bogorad PL. Regional measurement of the ^{3}He diffusion coefficient in the human lung. In: Proc 6th ISMRM Scientific Meeting, Sydney, 1998. p 1906.

120. Saam B, Yablonskiy DA, Gierada DS, Cooper JD, Lefrak SS, Conradi MS. Measuring diffusivity of ^{3}He in human lung: preliminary study of patients with emphysema. Eur Radiol 1999;9:B22.

121. Chen XJ, Hedlund LW, Möller HE, Chawla MS, Maronpot RR, Johnson GA. Detection of emphysema in rat lungs using magnetic resonance measurements of ^{3}He diffusion. Proc Natl Acad Sci USA 2000;97: 11478–11481.

122. Saam B, Yablonskiy DA, Kodibagkar VD, Leawoods JC, Gierada DS, Cooper JD, Lefrak SS, Conradi MS. MR imaging of diffusion of ^{3}He gas in healthy and diseased lungs. Magn Reson Med 2000;44:174–179.

123. Carman PC. Flow of gases through porous media. New York: Academic Press; 1956.

124. Mair RW, Cory DG, Peled S, Tseng CH, Patz S, Walsworth RL. Pulsed-field-gradient measurements of time-dependent gas diffusion. J Magn Reson 1998;135:478–486.

125. Mair RW, Wong GP, Hoffmann D, Hürlimann MD, Patz S, Schwartz LM, Walsworth RL. Probing porous media with gas diffusion NMR. Phys Rev Lett 1999;83:3324–3327.

126. Salerno M, Brookeman JR, Mugler JP. Time-dependent hyperpolarized ^{3}He diffusion MR imaging: initial experience in healthy and emphysematous lungs. In: Proc 9th ISMRM Scientific Meeting, Glasgow, 2001. p 950.

127. Crémillieux Y, Berthezene Y, Humblot H, Viallon M, Canet E, Bourgeois M, Albert T, Heil W, Briguet A. A combined ^{1}H perfusion/^{3}He ventilation NMR study in rat lungs. Magn Reson Med 1999;41:645–648.

128. Berthezene Y, Vexler V, Clement O, Muhler A, Moseley ME, Brasch RC. Contrast-enhanced MR imaging of the lung: assessments of ventilation and perfusion. Radiology 1992;183:667–672.

129. Hagspiel KD, Mugler JP, Altes TA, de Lange EE, Knight-Scott J, Munger TM, Berr SS, Mai VM, Daniel TM, Spellman MJ, Mata JF, Bogorad PL, Driehuys B, Gentile TR, Jones GL, Thompson AK, Brookeman JR. Static MR imaging of the airways using hyperpolarized ³He and ¹²⁹Xe: the University of Virginia experience. Eur Radiol 1999;9:B20.

130. Mai VM, Hagspiel KD, Altes T, Goode AR, Williams MB, Berr SS. Detection of regional pulmonary perfusion deficit of the occluded lung using arterial spin labeling in magnetic resonance imaging. J Magn Reson Imag 2000;11:97–102.

131. Roberts DA, Rizi RR, Lipson DA, Aranda M, Baumgardner J, Bearn L, Hansen-Flaschen J, Gefter WB, Hatabu HH, Leigh JS, Schnall MD. Detection and localization of pulmonary air leaks using laser-polarized ³He MRI. Magn Reson Med 2000;44:379–382.

132. Rizi RR, Roberts DA, Dimitrov IE, Schnall MD, Leigh JS. MRI of pulmonary ventilation/perfusion using hyperpolarized ³He gas and arterial spin-tagging: preliminary results in healthy subjects. In: Proc 6th ISMRM Scientific Meeting, Sydney, 1998. p 447.

133. Lipson DA, Dimitrov IE, Rizi RR, Gentile TR, Jones G, Thompson AK, Roberts DA, Pavelsky H, Gefter W, Schnall MD, Leigh JS, Hansen-Flaschen J. Noninvasive MRI ventilation/perfusion scanning using helium-3 and arterial spin-tagging in orthotopic lung transplant patients. In: Proc 7th ISMRM Scientific Meeting, Philadelphia, 1999. p 135.

134. Viallon M, Berthezène Y, Décorps M, Wiart M, Callot V, Bourgeois M, Humblot H, Briguet A, Crémillieux Y. Laser-polarized ³He as a probe for dynamic regional measurements of lung perfusion and ventilation using magnetic resonance imaging. Magn Reson Med 2000;44:1–4.

135. Swanson SD, Rosen MS, Coulter KP, Welsh RC, Chupp TE. Distribution and dynamics of laser-polarized ¹²⁹Xe magnetization in vivo. Magn Reson Med 1999;42:1137–1145.

136. Ruppert K, Brookeman JR, Hagspiel KD, Driehuys B, Mugler JP. NMR of hyperpolarized ¹²⁹Xe in the canine chest: spectral dynamics during a breath-hold. NMR Biomed 2000;13:220–228.

137. Kety SS. The theory and applications of the exchange of inert gas at the lungs and tissues. Pharmacol Rev 1951;3:1–41.

138. Peled S, Jolesz FA, Tseng CH, Nascimben L, Albert MS, Walsworth RL. Determinants of tissue delivery for ¹²⁹Xe magnetic resonance in humans. Magn Reson Med 1996;36:340–344.

139. Martin CC, Williams RF, Gao JH, Nickerson LDH, Xiong J, Fox PT. The pharmacokinetics of hyperpolarized xenon: implications for cerebral MRI. J Magn Reson Imag 1997;7:848–854..

140. Lavini C, Payne GS, Leach MO, Bifone A. Intravenous delivery of hyperpolarized ¹²⁹Xe: a compartmental model. NMR Biomed 2000; 13:238–244.

141. Swanson SD, Rosen MS, Agranoff BW, Coulter KP, Welsh RC, Chupp TE. Brain MRI with laser-polarized ¹²⁹Xe. Magn Reson Med 1997;38: 695–698.

142. Brown TR, Kincaid BM, Ugurbil K. NMR chemical shift imaging in three dimensions. Proc Natl Acad Sci USA 1982;79:3523–3526.

143. Bifone A, Song YQ, Seydoux R, Taylor RE, Goodson BM, Pietrass T, Budinger TF, Navon G, Pines A. NMR of laser-polarized xenon in human blood. Proc Natl Acad Sci USA 1996;93:12932–12936.

144. Wolber J, Cherubini A, Dzik-Jurasz ASK, Leach MO, Bifone A. Spin-lattice relaxation of laser-polarized xenon in human blood. Proc Natl Acad Sci USA 1999;96:3664–3669.

145. Wolber J, Cherubini A, Leach MO, Bifone A. On the oxygenation-dependent ¹²⁹Xe T_1 in blood. NMR Biomed 2000;13:234–237.

146. Albert MS, Kacher DF, Balamore D, Venkatesh AK, Jolesz FA. T_1 of ¹²⁹Xe in blood and the role of oxygenation. J Magn Reson 1999;140: 264–273.

147. Albert MS, Balamore D, Kacher DF, Venkatesh AK, Jolesz FA. Hyperpolarized ¹²⁹Xe T_1 in oxygenated and deoxygenated blood. NMR Biomed 2000;13:407–414.

148. Ruppert K, Mugler JP, Hagspiel KD, Altes TA, Mata JF, Brookeman JR, Driehuys B, Menon A, Kaza AK, Kron IL. Distinguishing extra- and intra-pulmonary gas using xenon polarization transfer contrast (XTC). In: Proc 9th ISMRM Scientific Meeting, Glasgow, 2001. p 2002.

149. Lassen NA, Lindbjerg J, Munck O. Measurement of blood-flow through skeletal muscle by intramuscular injection of xenon-133. Lancet 1964;i:686–689.

150. Goodson BM, Song YQ, Taylor RE, Schepkin VD, Brennan KM, Chingas GC, Budinger TF, Navon G, Pines A. In vivo NMR and MRI using injection delivery of laser-polarized xenon. Proc Natl Acad Sci USA 1997;94:14725–14729.

151. Goodson BM. Using injectable carriers of laser-polarized noble gases for enhancing NMR and MRI. Concepts Magn Reson 1999;11:203–223.

152. Möller HE, Chawla MS, Chen XJ, Driehuys B, Hedlund LW, Wheeler CT, Johnson GA. Magnetic resonance angiography with hyperpolarized ¹²⁹Xe dissolved in a lipid emulsion. Magn Reson Med 1999;41: 1058–1064.

153. Wolber J, Rowland IJ, Leach MO, Bifone A. Perfluorocarbon emulsions as intravenous delivery media for hyperpolarized xenon. Magn Reson Med 1999;41:442–449.

154. Venkatesh AK, Zhao L, Balamore D, Jolesz FA, Albert MS. Evaluation of carrier agents for hyperpolarized xenon MRI. NMR Biomed 2000; 13:245–252.

155. Duhamel G, Choquet P, Leviel JL, Steibel J, Lamalle L, Julien C, Kober F, Grillon E, Derouard J, Décorps M, Ziegler A, Constantinesco A. In vivo ¹²⁹Xe NMR in rat brain during intra-arterial injection of hyperpolarized ¹²⁹Xe dissolved in a lipid emulsion. CR Acad Sci III 2000; 323:529–536.

156. Duhamel G, Choquet P, Grillon E, Lamalle L, Leviel JL, Ziegler A, Constantinesco A. Xenon-129 MR imaging and spectroscopy of rat brain using arterial delivery of hyperpolarized xenon in a lipid emulsion. Magn Reson Med 2001;46:208–212.

157. Wolber J, McIntyre DJO, Rodrigues LM, Carnochan P, Griffiths JR, Leach MO, Bifone A. In vivo hyperpolarized ¹²⁹Xe NMR spectroscopy in tumors. Magn Reson Med 2001;46:586–591.

158. Chawla MS, Chen XJ, Möller HE, Cofer GP, Wheeler CT, Hedlund LW, Johnson GA. In vivo magnetic resonance vascular imaging using laser-polarized ³He microbubbles. Proc Natl Acad Sci USA 1998;95:10832–10835.

159. Chawla MS, Chen XJ, Cofer GP, Hedlund LW, Kerby MB, Ottoboni TB, Johnson GA. Hyperpolarized ³He microspheres as a novel vascular signal source for MRI. Magn Reson Med 2000;43:440–445.

160. Chawla MS, Cofer GP, Hedlund LW, Tajik JK, Kerby MB, Ottoboni TB, Johnson GA. Perfusion assessment using hyperpolarized ³He microspheres. In: Proc 8th ISMRM Scientific Meeting, Denver, 2000. p 10.

161. Callot V, Canet E, Brochot J, Viallon M, Humblot H, Briguet A, Tournier H, Crémillieux Y. MR perfusion imaging using encapsulated laser-polarized ³He. Magn Reson Med 2001;46:535–540.

162. Callot V, Canet E, Brochot J, Berthezène Y, Viallon M, Humblot H, Briguet A, Tournier H, Crémillieux Y. Vascular and perfusion imaging using encapsulated laser-polarized helium. MAGMA 2001;12:16–22.

163. Takahashi A, Hedlund LW, Chawla MS, Johnson GA. In vivo vascular imaging with hyperpolarized ³He in microspheres. In: Proc 9th ISMRM Scientific Meeting, Glasgow, 2001. p 307.

164. Callot V, Canet E, Brochot J, Humblot H, Briguet A, Tournier H, Crémillieux Y. Coronary MR imaging using laser-polarized helium3 microbubbles: preliminary results in isolated pig hearts. In: Proc 9th ISMRM Scientific Meeting, Glasgow, 2001. p 517.

165. Hedlund LW, Chen XJ, Chawla MS, Cofer GP, Cates G, Happer W, Wheeler CT, Johnson GA. Pulmonary airway obstruction in an animal model: MRI detection using hyperpolarized ³He. In: Proc 5th ISMRM Scientific Meeting, Vancouver, 1997. p 183.

166. Callaghan PT. Principles of nuclear magnetic resonance microscopy. Oxford: Clarendon Press; 1991.

167. Viallon M, Cofer GP, Suddarth SA, Möller HE, Chen XJ, Chawla MS, Hedlund LW, Crémillieux Y, Johnson GA. Functional MR microscopy of the lung using hyperpolarized ³He. Magn Reson Med 1999;41:787–792.

168. Guenther D, Eberle B, Hast J, Lill J, Markstaller K, Puderbach M, Schreiber WG, Hanisch G, Heussel CP, Surkau R, Grossmann T, Weiler N, Thelen M, Kauczor HU. ³He MRI in healthy volunteers: preliminary correlation with smoking history and lung volumes. NMR Biomed 2000;13:182–189.

169. Kauczor HU, Markstaller K, Puderbach M, Lill J, Eberle B, Hanisch G, Grossmann T, Heussel CP, Schreiber W, Thelen M. Volumetry of ventilated airspaces by ³He MRI. Preliminary results. Invest Radiol 2001;36:110–114.

170. Rizi RR, Baumgardner JE, Saha PK, Aranda M, Asaii A, Frazer M, Roberts DA, Schnall MD, Leigh JS. Regional lung compliance by hyperpolarized ³helium magnetic resonance imaging. In: Proc 9th ISMRM Scientific Meeting, Glasgow, 2001. p 944.

171. Kauczor HU, Ebert M, Kreitner KF, Nilgens H, Surkau R, Heil W, Hofmann D, Otten EW, Thelen M. Imaging of the lungs using ³He MRI: preliminary clinical experience in 18 patients with and without lung disease. J Magn Reson Imag 1997;7:538–543.

172. Mata J, Altes T, Christopher J, Mugler J, Brookeman J, de Lange E. Positional dependence of small inferior ventilation defects seen on hyperpoarized helium-3 MR of the lung. In: Proc 9th ISMRM Scientific Meeting, Glasgow, 2001. p 949.

173. Altes TA, Powers PL, Knight-Scott J, Rakes G, Platts-Mills TAE, de Lange EE, Alford BA, Mugler JP, Brookeman JR. Hyperpolarized ^{3}He MR lung ventilation imaging in asthmatics: preliminary findings. J Magn Reson Imag 2001;13:378−384.

174. Kauczor HU, Surkau R, Roberts T. MRI using hyperpolarized noble gases. Eur Radiol 1998;8:820−827.

175. Altes T, Froh DK, Salerno M, Cook CD, Mata J, Mugler JP, de Lange EE, Brookeman JR. Hyperpolarized helium-3 MR imaging of lung ventilation changes following airway mucus clearence treatment in cystic fibrosis. In: Proc 9th ISMRM Scientific Meeting, Glasgow, 2001. p 2003.

176. McAdams HP, Palmer SM, Donnelly LF, Charles HC, Tapson VF, MacFall JR. Hyperpolarized ^{3}He-enhanced MR imaging of lung transplant recipients: preliminary results. Am J Roentgenol 1999;173:955−959.

177. Kauczor HU, Eberle B, Lill J, Schreiber W, Hanisch G, Markstaller K, Guenther D, Diergarten T, Weiler N. Funktionelle Strategien zur Untersuchung der Ventilation bei einseitig Lungentransplantierten mittels Helium-3 MRT. RöFo. Fortschr Geb Röntgenstr Neuen Bildgeb Verfahr 2000;172:S16.

178. Schreiber WG, Weiler N, Kauczor HU, Markstaller K, Eberle B, Hast J, Surkau R, Großmann T, Deninger A, Hanisch G, Otten EW, Thelen M. Ultraschnelle MRT der Lungenventilation mittels hochpolarisiertem Helium-3. RöFo. Fortschr Geb Röntgenstr Neuen Bildgeb Verfahr 2000;172:129−133.

179. Gierada DS, Saam B, Yablonskiy D, Cooper JD, Lefrak SS, Conradi MS. Dynamic echo planar MR imaging of lung ventilation with hyperpolarized ^{3}He in normal subjects and patients with severe emphysema. NMR Biomed 2000;13:176−181.

180. Salerno M, Altes TA, Brookeman JR, de Lange EE, Mugler JP. Dynamic spiral MRI of pulmonary gas flow using hyperpolarized ^{3}He: preliminary studies in healthy and diseased lungs. Magn Reson Med 2001;46:667−677.

181. Salerno M, Brookeman JR, de Lange EE, Knight-Scott J, Mugler JP. Detection of regional microstructural changes of the lung in emphysema using hyperpolarized ^{3}He diffusion MRI. In: Proc 8th ISMRM Scientific Meeting, Denver, 2000. p 9.

182. Salerno M, de Lange EE, Altes TA, Truwit JD, Brookeman JR, Mugler JP. Emphysema: Hyperpolarized helium 3 diffusion MR imaging of the lungs compared with spirometric indexes—initial experience. Radiology 2002;222:252−260.

183. Hanisch G, Schreiber W, Diergarten T, Markstaller K, Eberle B, Kauczor HU, Großmann T, Thelen M. Investigation of intrapulmonary diffusion by ^{3}He MRI. Eur Radiol 2000;10:345.

184. Edelman RR, Hatabu H, Tadamura E, Li W, Prasad PV. Noninvasive assessment of regional ventilation in the human lung using oxygen-enhanced magnetic resonance imaging. Nat Med 1996;2:1236−1239.

185. Rinck PA, Petersen SB, Lauterbur PC. NMR-Imaging von fluorhaltigen Substanzen. RöFo. Fortschr Geb Röntgenstr Neuen Bildgeb Verfahr 1984;140:239−243.

186. Kuethe DO, Caprihan A, Fukushima E, Waggoner RA. Imaging lungs using inert fluorinated gases. Magn Reson Med 1998;39:85−88.

187. Kuethe DO, Caprihan A, Gach HM, Lowe IJ, Fukushima E. Imaging obstructed ventilation with NMR using inert fluorinated gases. J Appl Physiol 2000;88:2279−2286.

188. Schreiber WG, Eberle B, Laukemper-Ostendorf S, Markstaller K, Weiler N, Scholz A, Bürger K, Heussel CP, Thelen M, Kauczor HU. Dynamic ^{19}F-MRI of pulmonary ventilation using sulfur hexafluoride (SF$_6$) gas. Magn Reson Med 2001;45:605−613.

189. Wolber J, Cherubini A, Leach MO, Bifone A. Hyperpolarized ^{129}Xe NMR as a probe for blood oxygenation. Magn Reson Med 2000;43:491−496.

190. Spence MM, Rubin SM, Dimitrov IE, Ruiz EJ, Wemmer DE, Pines A, Yao SQ, Tian F, Schultz PG. Functionalized xenon as a biosensor. Proc Natl Acad Sci USA 2001;98:10654−10657.

191. Driehuys B, Cates GD, Happer W, Mabuchi H, Saam B, Albert MS, Wishnia A. Spin transfer between laser-polarized ^{129}Xe nuclei and surface protons. Phys Lett A 1993;184:88−92.

192. Bowers CR, Long HW, Pietrass T, Gaede HC, Pines A. Cross polarization from laser-polarized solid xenon to ^{13}CO$_2$ by low-field thermal mixing. Chem Phys Lett 1993;205:168−170.

193. Navon G, Song YQ, Room T, Appelt S, Taylor RE, Pines A. Enhancement of solution NMR and MRI with laser-polarized xenon. Science 1996;271:1848−1851.

194. Song YQ. Spin polarization-induced nuclear Overhauser effect: an application of spin-polarized xenon and helium. Concepts Magn Reson 2000;12:6−20.